Dynamic Anapole: Realization by Metasurfaces made of Sculptured and Water-based Cylinders

Author: Takou Evangelia

Supervisors:

Eleftherios N. Economou

Konstantinos Makris

Physics Department

University of Crete

May 27, 2019

ACKNOWLEDGMENTS

I would like to thank my thesis advisor Eleftherios N. Economou, Professor Emeritus of the Physics Department at the University of Crete and Head of the Photonic- Phononic- and Metamaterials group at FORTH IESL. Prof. Economou has been constantly providing me with valuable assistance, careful guidance and has enhanced my admiration toward the field of Condensed Matter Physics. His prominent insight in physics and influential teaching capabilities, allowed me to broaden my knowledge in physics and he had a major impact on my motivations and field of interest. He has also supported me extensively in many aspects and welcomed me to be part of his group, for which I am grateful to him.

I would also like to acknowledge two distinguished researchers and members of the PPM group, Dr. Tasolamprou Anna and Dr. Tsilipakos Odysseas. Their hard work, consistency and dedication in research has instilled in me the sense of responsibility and discussions with them have further stimulated my interests. They willingly introduced me to the fundamental tools of research and shared their knowledge with me so as to take a step further. For that, I thank you both sincerely for the excellent cooperation and guidance throughout the entire process.

Furthermore, I would like to deeply thank Dr. George Kenanakis and Dr. Zacharias Viskadourakis, again members of the PPM group, for allocating important amount of their time to design in detail the water-based structure and conduct a relevant experiment.

In addition, I would like to thank my family for always been there for me, and especially my older brother and room-mate for the past five years, Efthymis, for assisting me in all my life circumstances.

Abstract

This thesis consists of two main parts: 1) A presentation of all-dielectric polaritonic metasurfaces consisting of properly sculptured cylinders to sustain the dynamic anapole, i.e. a non-radiating alternating current distribution. This part is an attachment of a paper of which I am the first author, and was recently submitted in Physical Review B [a]. In the paper, two ways for the anapole to emerge are examined; first, by combining modes based on the first and the fourth *mixed toroidal* Mie resonance of a cylinder made of high permittivity $LiTaO_3$ and second, by breaking the circular symmetry, enabling substantial toroidal dipole to emerge from the *magnetic quadrupole* Mie mode. In both designs, the circular cross-section of each cylinder varies periodically along its length in a binary way, from small to large, while its overall circular symmetry has to be broken in order to remove parasitic magnetic modes. Segments of small cross-sections are the main source of the *electric dipole* Mie mode, while large cross-section segments sustain the fourth, *mixed toroidal dipole* Mie mode (in the first design) or the hybrid *magnetic quadrupole* Mie mode (in the second design). The sensitivity of the anapole states to the material dissipation losses is examined leading to the conclusion that the proposed metasurfaces offer a scheme for realistically implementing the anapole in the low THz. 2) Another practical and convenient way for the realization of the dynamic anapole, is to exploit the dielectric properties of water. Being a polar material of adjustable characteristics, water can lead to novel applications, by being incorporated into a many-rod metasurface. The theoretical results evaluate the resilience of the anapole state achieved by a *collective toroidal super-mode* for implementation in the low GHz; a widely-established and accurate in the low GHz, Debye model for the water permittivity was used. The theory is further supported by an experiment conducted in one of the labs at Forth IESL, and then the comparison of theory and experiment is examined concluding to their good agreement, opening thus the path for the utilization of water in various applications.

[a] Evangelia Takou, Anna C. Tasolamprou, Odysseas Tsilipakos and Eleftherios N. Economou. "Dynamic Anapole in Metasurfaces made of Sculptured Cylinders". *Phys. Rev*. **B** (submitted).

CONTENTS

I. INTRODUCTION

Non-radiating sources have attracted strong interest both from the fundamental point of view of electrodynamics and for the applications of non-scattering objects [1, 2]. A type of non-radiating source that attracts increasing attention in the photonic community is the dynamic anapole, which is usually created by the superposition of electric and toroidal dipole moments [3, 4]. The toroidal dipole is a peculiar excitation that differs from the familiar electric and magnetic dipoles; the latter involve back-and-forth currents and closed circulation of currents respectively; the pure toroidal dipole rises from the poloidal currents circulating on a surface of a torus along its meridians. In spite of these quite different current distributions, both the electric and the toroidal dipoles emit radiation with the same angular momentum and parity properties, rendering their radiation pattern indistinguishable for any distant observer [5]; this is one of the reasons that toroidal multipoles are not considered in classical electrodynamics textbooks [6, 7]; it is also the reason that electric and toroidal dipoles appear to be ideal for destructive interference and, hence, for the realization of the dynamic anapole, although it is quite difficult to match their strengths and isolate them from adjacent contributions. The evolution of metamaterials, artificial materials with engineered macroscopic electromagnetic properties, has provided the tool for overcoming this last difficulty [8] and for the realization of the dynamic anapole, the nontrivial, non-radiating source which is the objective of the present work.

As it was mentioned before, the dynamic anapole can be created by a toroidal dipole (**T**) oscillating out of phase relative to the electric dipole (**p**) leading thus to destructive interference of the radiated field in the far-field zone. The relation that guarantees this interference reads:

$$\mathbf{p} + ik\mathbf{T} = 0 \tag{1}$$

where $k = \omega/c$. Although in the far-field region the fields vanish, this is not the case for the source region; this is due to the fact that the difference of the vector potentials $\mathbf{A}_{\mathrm{T}}(\mathbf{r},t)$ and $\mathbf{A}_{\mathrm{p}}(\mathbf{r},t)$ of a toroidal and an electric dipole emission, respectively, cannot be eliminated via a gauge transformation. More explicitly, if one considers point-like sources (as there is no limitation upon the size of the source) of electric and toroidal dipoles superimposed under the relation of Eq. (1), the corresponding vector potential $\Delta\mathbf{A} = \mathbf{A}_{\mathrm{T}} - \mathbf{A}_{\mathrm{p}}$ reads:

$$\Delta\mathbf{A} = \nabla\left(\mathbf{T}\cdot\nabla\left(\frac{e^{ikr}}{r}\right)\right) + 4\pi\delta^3(\mathbf{r})\cdot\mathbf{T} \tag{2}$$

The second term in the expression for the net vector potential is not-trivial, since it does not vanish upon application of the curl. In other words, this indicates that the net vector potential cannot be eliminated at all points in space in any gauge [9]. In the static case, $k = 0$, the electric dipole moment disappears, $\mathbf{p} = 0$, making the static anapole synonymous with the static toroidal dipole. It has been argued that the point dynamic anapole may be viewed as the basic building block out of which an arbitrary non-radiating source can be composed of [10].

The first anapole state was verified experimentally in the GHz spectrum using metallic split ring resonators [11]. Simpler geometries followed and the first experimental observation of the dynamic anapole in the visible, in a stand alone dielectric particle (Si nanodisk), was reported in [12], as well as in structures of core-shell nanowires [13] and in spheres [14]. Hybrid situations of coexisting magnetic and electric anapole states have also been investigated for the case of a high index spherical particle [15]. The non-radiating response of the anapole modes accompanied by the enhanced near fields has found numerous applications such as in cloaking [16], harmonic generation [17–19], nanoscale lasers [20], high Q factor devices [21], sensing [22, 23], Raman scattering enhancement [24] and many more. The far field extinction combined with the maximized electromagnetic energy concentration within the nanostructures has also opened the possibility of intensity enhancement in all-dielectric nanostructures [12, 25, 26], which was accomplished by utilizing Si nanodisks (slotted in the latter case).

Most of the works discussing the anapole excitation in metamaterials involve the manipulation of the toroidal moment through various structural schemes. Metallic metamaterials with asymmetric inclusion, like asymmetric metallic bars [27] or properly adjusted in U-shaped metaatoms [28] have been proven to provide control over the toroidal excitation. Also in the case of all-dielectric metamaterials control over the toroidal excitation has been provided by the shape, size and formation of the nanoparticles, for example the size of silicon disks [12, 21], the formation of silicon fins [29], the number, shape and formation of infinite length polaritonic rods [30–34] etc. Remarkably, it has been also recently realized that toroidal dipole moment exists within the natural TE_{01} mode (fourth mode in ascending frequency) of an infinite length single cylinder [13, 31, 35]. The toroidal dipole moment in this mode is accompanied by a strong electric dipole moment due to the asymmetric positive and negative polarization currents.

In the recent years, water has attracted great interest as a result of its outstanding potential as an alternative form of a high-refractive-index material. The two prominent properties of water are its convenience to adjust to the shape of its container enabling thus the manufacture of a wide range of water-based objects, as well as the strong temperature dependence of its dielectric function. Water also prevails over the scarce and expensive high-index materials such as Barium Strontium Titanate of Lithium Tantalate. Many recent researches exploit the advantages of water, opening the path for numerous applications in tunable all-dielectric photonic structures and metamaterials. Examples of the tunability properties of water are its thermal, mechanical and gravitational ones exploited in periodically positioned water-filled reservoirs [36]. Magnetic field enhancement of MRI coils has been accomplished by controlling the water level in a tuning cavity of a spiral resonator [37]. The dielectric properties of water also enabled it to be developed as a dielectric spacer in the substrate of metal-backed metamaterial absorbers, achieving thus a broadband performance of the absorbers [38]. Enhanced broadband microwave absorption was also reported in [39], while the guiding effects of water-filled elements were investigated in [40]. Recently, it was proven in [41] that water offers control over the Mie resonances; water cubes were

found to sustain thermally tunable magnetic and electric dipole resonances. Thus, it is clear that water is becoming an excellent and competitive candidate for controllability, as is covers effectively a wide range of practical applications.

The two parts of the thesis are organized as follows: In Sec. II A, the modes sustained by an infinite and uniform cylinder are presented and an electromagnetic characterization is performed with a focus on the electric and mixed toroidal dipole character. These modes are properly modified by our design of a sculptured cylinder (with the binary distribution of its cross-section) serving as the building block for the proposed metasurface. In Sec. II B we present the simulation results of the reflection power by the metasurface designed to sustain the anapole state due to the mixed toroidal and the electric dipole modes. In Sec. II C we discuss the structure's sensitivity to the dissipation losses. In Sec. II D we present the design principles, implementation, and dissipation losses sensitivity of a modified metasurface based on a toroidal component emerging from quadrupole-like Mie mode and electric dipole and then the first part of the work is concluded. In Sec. III A a short discussion is provided for the many-rod configurations and the collective toroidal super-modes, that emerge when more than one cylinders are combined in a unit cell. In Sec. III B, a theoretical analysis is preformed for two water-based systems, while in Sec. III C the experiment is described regarding a water-filled system of five rods and the comparison of the experiment with the theory is evaluated.

II. METASURFACES MADE OF SCULPTURED CYLINDERS

A. Mixed electric and toroidal modes of a cylinder and principles of design

We investigate the possibility of a dynamic anapole by considering a metasurface consisting of dielectric cylinders; the circular cross-section of each of them varies periodically along its length in a binary way as shown in Fig. 1(c). The values of the small and the large cross-sections as well as their corresponding lengths are to be fixed in such a way as to satisfy the anapole condition of Eq. (1), as accurately as possible. We begin the study by focusing on the Mie eigenmodes of an isolated polaritonic cylinder, infinite and uniform along its length coinciding with the $\hat{\mathbf{z}}$-axis direction [Fig. 1(a)]. We assume E_z polarization and eigensolutions whose wavevector remains strictly in the xy plane, $k_z = 0$. Initially we consider that the radius of the infinite $LiTaO_3$ rod is equal to $R_c = 15$ μm. We have chosen the $LiTaO_3$ polaritonic material to drastically reduce the ohmic losses while maintaining high permittivity. In a polaritonic material the induced polarization currents are due to the AC motions of the cations and the anions; their dielectric function has the form:

$$\epsilon(\omega) = \epsilon_1 + i\epsilon_2 = \epsilon_\infty \frac{\omega_L^2 - \omega^2 - i\omega\gamma}{\omega_T^2 - \omega^2 - i\omega\gamma} \tag{3}$$

$$\epsilon(0) \equiv \epsilon_0 = \epsilon_\infty \left(\frac{\omega_L}{\omega_T}\right)^2 \tag{4}$$

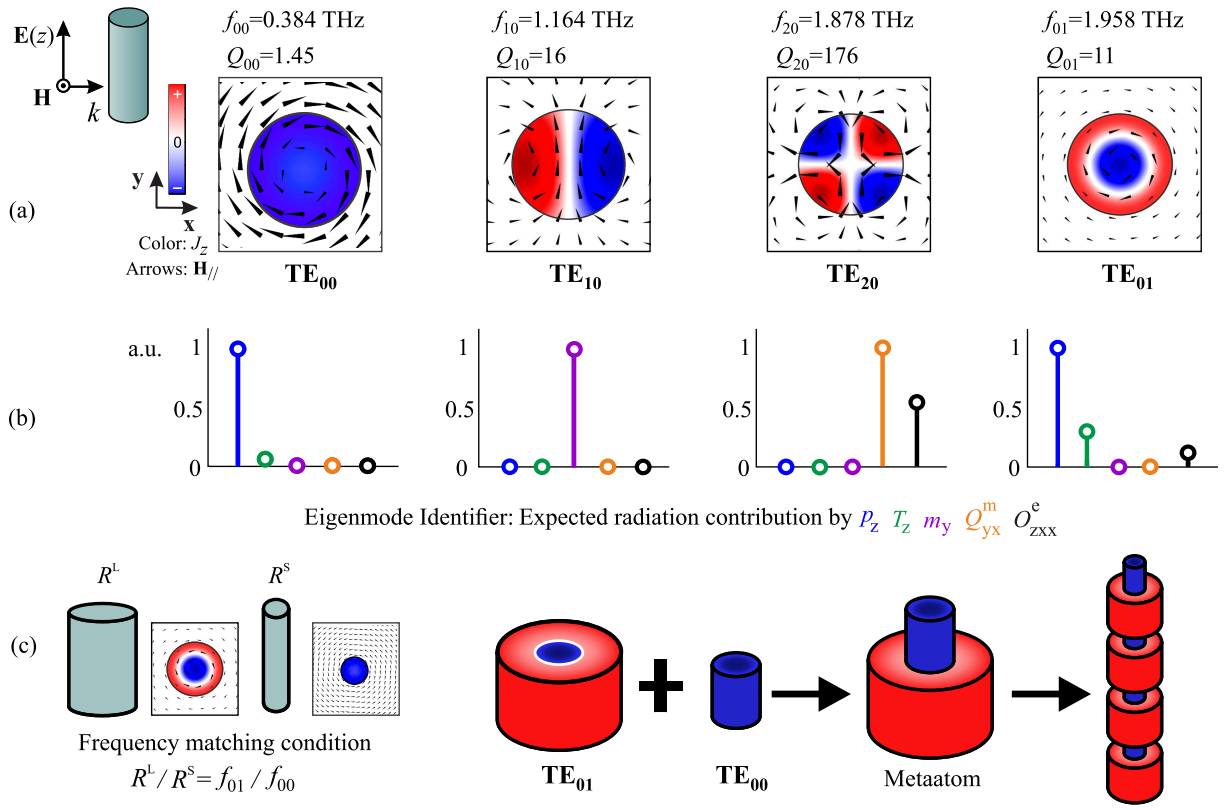

FIG. 1. (a) First four transverse electric eigenmodes of a single infinite length and uniform circular cross-section polaritonic rod: polarization current distribution J_z (color), magnetic field lines (arrows), resonant frequency and quality factor are shown. (b) Eigenmode identifier regarding the contributions coming from the electric dipole moment p_z, the toroidal dipole moment T_z, the magnetic dipole moment m_y, the magnetic quadrupole moment Q^m_{yx} and the electric octupole moment O^e_{zxx}; these radiation contributions are normalized in terms of the dominant one in each mode individually. The character of the shown modes is: TE$_{00}$, electric dipole; TE$_{10}$, magnetic dipole; TE$_{20}$, magnetic quadrupole; and TE$_{01}$, *mixed* toroidal dipole; the term *mixed* is adopted since both electric and toroidal dipoles participate in the eignemode, in spite the fact that the magnetic field lines suggest a predominantly toroidal moment. (c) The unit cell of each cylinder (the so called metaatom) consists of two cylindrical pieces one of smaller and the other of larger cross-section such that the TE$_{00}$ eigenfrequency of the first to coincide with the TE$_{01}$ eigenfrequency of the second, opening thus the path for the realization of the dynamic anapole.

For $LiTaO_3$ the transverse optical resonance frequency is $\omega_T/2\pi = 26.7$ THz, the longitudinal resonance frequency is $\omega_L/2\pi = 46.9$ THz, $\epsilon_\infty = 13.4$ and $\gamma/2\pi = 0.94$ THz, with the static permittivity equal to $\epsilon_0 = 41.34$. In the low THz regime, the dielectric function has a real constant value of $\epsilon_1 \sim 41$, while the dissipation losses are in the order of few 10^{-3}. The dissipation losses are low enough to be considered negligible for our initial investigation; extensive study of the structures sensitivity to losses is provided in Sects. II C and II D.

Figure 1(a) presents the E_z polarized Mie eigenmodes in ascending frequency, the polar-

ization current distribution, the resonant frequency and the quality factor, sustained by an isolated, free-space standing, $LiTaO_3$ cylinder of radius $R_c = 15$ μm and permittivity $\epsilon_1 = 41$. They are calculated by eigenvalue analysis with the general purpose full wave, finite element based solver [42]. Figure 1(b) presents an electromagnetic character identification of each mode which is attained by calculating the dominant expected radiation contributions (amplitude) by the multipole moments in each eigenmode. Multipole moments are vectorial functions of the spatial distribution of polarization currents with expressions that incorporate the toroidal multipoles found in Refs. [34, 43] (Appendix C of Ref. [43]). Essentially, they describe the electromagnetic character (electric, magnetic, toroidal) of the local sources that are created by the circulation of alternating currents. In this case, the only nonzero component of the polarization current is J_z and the nonzero multipole radiation contributions come from the electric dipole moment p_z, the toroidal dipole moment T_z, the magnetic dipole moment m_y, the magnetic quadrupole moment Q^m_{yx}, and the electric octupole moment O^e_{zxx}. There is also an additional contribution coming from the electric quadrupole moment Q^e_{xz}, which in the two-dimensional space coincides with the magnetic dipole moment m_y and is therefore omitted from Fig. 1(b). Note also that the vector components depend on the rotational symmetry of the modes and the reference cartesian unit system as defined in Fig. 1(a). They are both selected to match the metasurface set up of Sec. II B. In Fig. 1(b), in each individual eigenmode the expected radiation contributions by the multipoles are normalized in terms of the dominant contribution. As seen in Figs. 1(a) and 1(b) the first mode, TE_{00} (subscript denoting zero radial and zero azimuthal variation), corresponds to the electric dipole and exhibits a very low quality factor $Q_{00} \sim 1.5$ which means that, when excited, is expected to strongly radiate in a broad frequency range. It is characterized by a strong electric dipole moment contribution from p_z and a residual toroidal dipole moment contribution from T_z. The next mode, TE_{10} (subscript denoting one azimuthal and zero radial variation), is the magnetic dipole with $Q_{10} = 16$ and is characterized by a strong contribution coming from m_y alone. Next in frequency is the TE_{20} magnetic quadrupole with a distinct magnetic quadrupole moment signature and a high quality factor $Q_{20} \sim 176$; in this case the dominant expected contribution comes from Q^m_{yx}, but at the same time there is a strong contribution that comes from O^e_{zxx}. The fourth mode is TE_{01}, with a zero azimuthal and one radial variation and a low quality factor $Q_{01} \sim 11$ indicative of its radiative nature. As seen in Fig. 1(b), the radiation contribution is expected to come mainly from the electric dipole p_z and secondarily from the toroidal dipole T_z; therefore it is denoted as mixed toroidal dipole in spite the fact that the magnetic lines suggest a predominantly toroidal dipole moment.

The idea behind achieving the anapole in this system is to match the eigenfrequencies of the mixed toroidal dipole mode TE_{01} and the electric dipole mode TE_{00}. This can be achieved by properly adjusting the diameter of the two sections in the binary metaatom, as presented in Fig. 1(c), in such a way that the radiation by the electric dipole p_z and the toroidal dipole T_z cancels out. The extra degree of freedom offered by the height of the two sections will be used in our goal to obtain the dynamic anapole. In the system

discussed here, where the rod is isolated in free-space and only dielectric materials with very low or no dispersion are involved, the frequency varies directly with the size of the rods. Therefore, the matching of the TE_{00} and TE_{01} mode occurs in cylinders with ratio of the two cross-sectional radii approximately equal to the ratio of the TE_{00} and TE_{01} frequencies $R_S/R_L \sim 1/5$. The subscripts '*S*', '*L*' stand for the small and large cross-section that sustain the TE_{00} and TE_{01}, respectively.

B. The anapole as a combination of electric and toroidal dipole modes in the dielectric metasurface

Using the sculptured cylinders with the periodic binary cross-section as building blocks, we construct the metasurface shown in Fig. 2. The radius of the small cross-section and the large cross-section areas are R_S, R_L respectively and the corresponding heights are H_S and H_L. The period along the $\hat{\mathbf{y}}$-axis is equal to $d = 40$ μm. A linearly polarized ($\mathbf{E}$ parallel to $\hat{\mathbf{z}}$-axis) plane wave impinges normally on this metasurface provoking the generation of currents that modify the scattered far-field as expressed in the transmission and reflection coefficients. Our goal is to achieve the dynamic anapole initially by manipulating the electric and mixed toroidal dipole moments; as far as the latter is concerned, we enhance its contribution by increasing the relevant volume of the larger cross-section [sustaining TE_{01} as depicted in Fig. 1(a) and 1(c)], while remaining in the subwavelength regime. In fact, if the '*S*' and '*L*' lengths are equal the electric dipole fully dominates the response; to remedy this, the TE_{00}-sustaining section has to be much shorter, compared to the TE_{01}-sustaining section.

We begin our investigation by assuming the non-optimized values of the design parameters for the metasurface: $H_L = 6$ μm, $H_S = 1$ μm, $R_L = 15$ μm and $R_S = 3$ μm and $d = 40$ μm. The ratio between the large '*L*' and small '*S*' cross-section ensures the spectral matching for the electric and mixed toroidal dipole modes. It should be noted here that the periodicity along the $\hat{\mathbf{y}}$-axis and the $\hat{\mathbf{z}}$-axis corrugation is expected to change the landscape of the sustained eigenmodes, their properties and moments identification with respect to the isolated cylinder of Fig. 1. However, certain aspects such as some relative spectral positions, the radiation trends and the current distributions of the electric, magnetic and toroidal modes still survive. In Fig. 3(a), the eigenfrequencies (both real, f, and imaginary parts, f'') of the $k_y = k_z = 0$ eigenmodes of the whole metasurface, shown in Fig. 2, are presented together with the current distributions of these eigenmodes within the metaatom part [see Fig. 1(c)]; although the eigenfrequencies have been shifted considerably relative to the values of a single uniform cylinder [shown in Fig. 1(a)], the current distributions are still, surprisingly, almost identical to those of a single uniform cylinder. In fact, we used the same names and the same notations for the eigenmodes of the metasurface as for those of a single uniform cylinder. Notice also that due to the electromagnetically small size of the cylinders height ($H_L \sim \lambda_n/2.5$, $H_S \sim \lambda_n/15$, where λ_n is the wavelength within the dielectric atom, $\lambda_n = \lambda_0/n = 15$ μm for $f = 3$ THz), the corresponding modes have no considerable variation

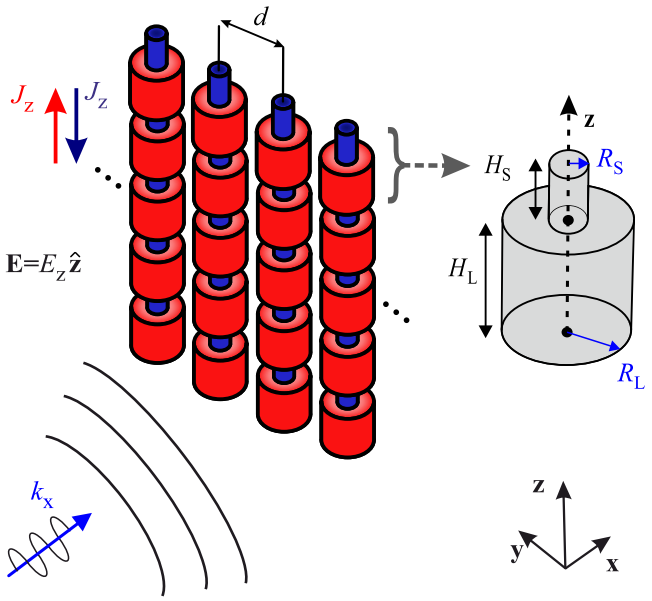

FIG. 2. Schematic representation of a metasurface composed by periodically repeating along the $\hat{\mathbf{y}}$-axis the sculptured cylinder shown in Fig. 1(c). The incident wave is $\hat{\mathbf{z}}$-polarized and normal incidence along the $\hat{\mathbf{x}}$-axis is assumed. The parameters for the small and large cross-sections of the unit cell are radii, R_S and R_L and heights H_S and H_L, respectively.

in the $\hat{\mathbf{z}}$-axis direction and this is the reason that they are denoted as TE_{mn0} [i.e. the third subscript referring to the $\hat{\mathbf{z}}$-axis (axial) variation is zero]; thus TE_{100} is the notation for the magnetic dipole, TE_{000}/TE_{010} for the mixed toroidal (or, more accurately, for the combined electric dipole and mixed toroidal), and TE_{200} for the quadrupole.

Figure 3(b) presents the reflected power associated with the excited multipoles by a plane wave normally incident on the metasurface. The reflected power from each multipole is a function of the incident wave induced polarization currents at each frequency and adds up to the total reflected field [34, 43]. The multipole moments that contribute mainly to the scattered field are: the electric dipole moment, p_z, the magnetic dipole moment m_y, the toroidal dipole moment T_z, the electric quadrupole Q^e_{xz}, the magnetic quadrupole Q^m_{yx} and the electric octupole O^e_{zxx} (in this $\hat{\mathbf{z}}$-dependent metaatom, Q^e_{xz} is not identical to m_y as in the $\hat{\mathbf{z}}$-independent case). There is also some weak contribution from Q^T_{xz} and O^m_{yxx} (not shown here). A surprise comes by comparing the eigenvalues of the metasurface shown in the data of Fig. 3(a) with the data of Fig. 3(b). A normally incident plane wave is expected to excite the eigenmodes of the metasurface possessing the same $\mathbf{k}$ character and hence local extrema in the reflected power contributions are expected to appear at these eigenfrequencies. Instead, this occurs only for the magnetic quadrupole excited mode which exhibits a prominent peak at its eigenfrequency at 3.6 THz; however, no peaks appear in Fig. 3(b) either at the magnetic dipole eigenfrequency (2.374 THz) or at the mixed toroidal eigenfrequency (2.723 THz); a possible explanation of this unexpected feature can be attributed to the very large imaginary parts of the eigenfrequencies of these eigenmodes which ap-

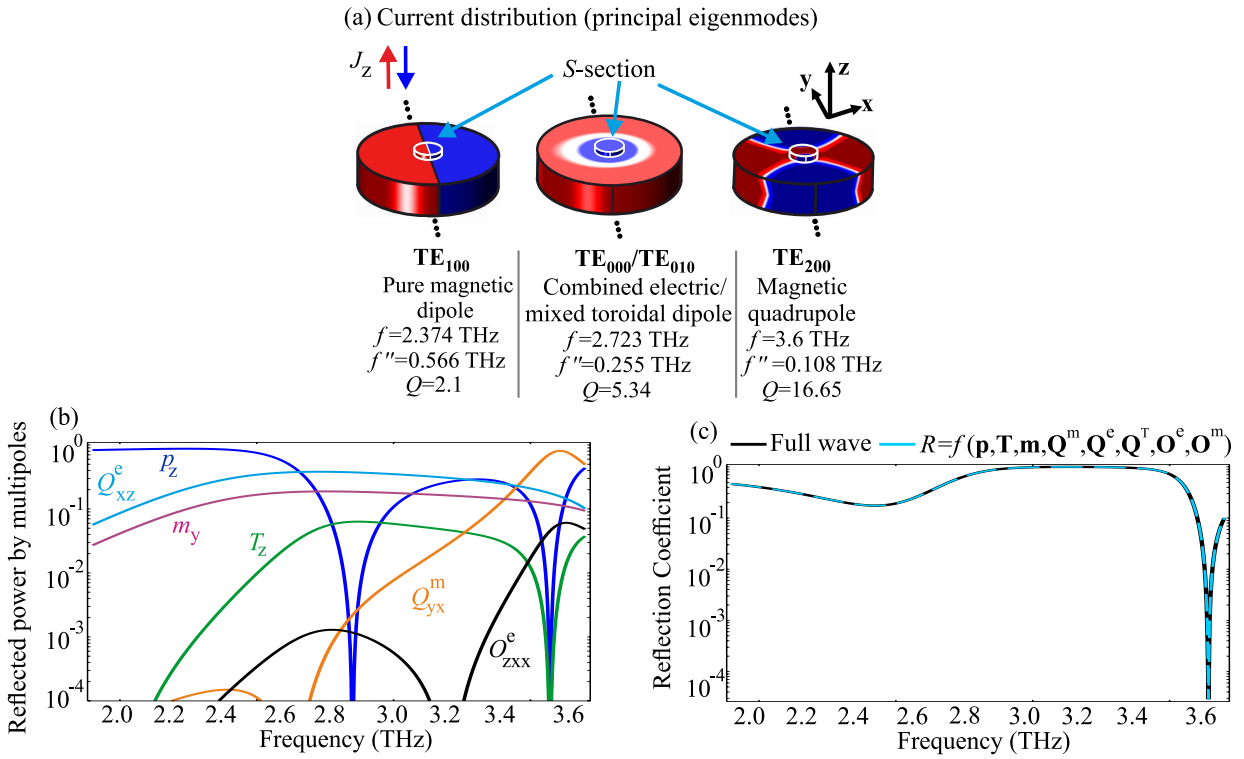

FIG. 3. (a) Eigenfrequencies (real and imaginary parts), and polarization current distributions of the $k_y = k_z = 0$, $\mathbf{E} = E_z\hat{\mathbf{z}}$ eigenmodes in the metaatom part of the whole metasurface as shown in Fig. 2; the shown eigenmodes are the pure magnetic dipole TE_{100}, the mixed toroidal TE_{010} and the magnetic quadrupole TE_{200}. (b) Reflected power contributions by the individual moments; notice the significant strength and the almost coincidence of the contributions of the magnetic dipole m_y and electric quadrupole Q^e_{xz}. (c) Reflection coefficients for the frequency range 1.9-3.7 THz calculated by the full wave analysis and the summation of all the amplitude contributions. Notice that the reflection dip occurs close to the electric and the toroidal dipole dips, indicating that the magnetic dipole/quadrupole and the electric quadrupole/octupole cancel out at the frequency of the reflection dip.

parently round-off the expected peaks. In Fig. 3(c) the total reflection coefficient in the frequency range 1.9-3.7 THz has been calculated by two methods: (i) by numerical full wave simulations based on the finite element method [42] and (ii) by the summation of the various multipole amplitudes that contribute to the reflected field. The agreement between the full wave numerical simulation and the analytical multipole expansion formulation is excellent as shown in Fig. 3(c) (validating thus the imperative presence of the toroidal dipole in the multipole expansion).

Returning to the fact that the imaginary parts of the eigenfrequencies of the magnetic dipole and the mixed toroidal dipole are very large (implying that the corresponding Q factors are very small), we stress that this holds to even larger degree for the electric dipole eigenmode associated with the larger section of the metaatom in spite of its much lower

eigenfrequency. As a result of the consequent broadness of these eigenmodes, their contribution to the reflection is substantial even for frequencies far away from their eigenfrequencies. With that in mind, we may interpreter the results of Fig. 3(b): There is a broad spectral region of magnetic dipole/electric quadrupole m_{y} and $Q^{\mathrm{e}}_{\mathrm{xz}}$ dominance which comes from the highly radiating magnetic dipole eigenmode with resonance at 2.374 THz, possessing the second lowest Q factor (after the electric dipole). The spectral signature of the electric dipole contribution p_{z} is more complicated due to the low Q factor of the electric dipole sustained in each of the two sections of the metaatom shown in Fig. 1(c), as well as the electric dipole character that is found in many excited modes originating from the uneven distribution of upward and downward currents. In Fig. 3(b), we notice two electric dipole, p_{z}, reflection dips. As mentioned, there is a large p_{z} tail coming from, the much lower in frequency TE_{000} mode associated with the L section of the unit cell which is very broad (due to its very low Q-factor) and thus overlaps with the frequency region of 2-3 THz. The combined TE_{000}/TE_{010} has also at the S section of the metaatom a pure electric dipole moment [and an electric dipole moment at the L section, see Fig. 1(b) associated with the TE_{01} eigenmode]. All these electric dipole contributions coming from different eigenmodes suffer a destructive interference at frequencies around 2.85 THz and 3.55 THz. The first dip comes mainly from the electric dipole contribution of the combined TE_{000}/TE_{010}. The second dip in the electric dipole contribution occurs around the magnetic quadrupole excited mode, at 3.6 THz, and is expected to be due, besides the TE_{200} and the combined TE_{000}/TE_{010}, to higher frequency excited modes as well. The signature of the magnetic quadrupole $Q^{\mathrm{m}}_{\mathrm{yx}}$ (accompanied by the electric octupole $O^{\mathrm{e}}_{\mathrm{zxx}}$) is more clear since it appears dominantly in the spectral vicinity of the TE_{200} excited mode and exhibits a high Q factor as seen from the sharp $Q^{\mathrm{m}}_{\mathrm{yx}}$ (and $O^{\mathrm{e}}_{\mathrm{zxx}}$) resonance at 3.6 THz.

For the realization of the anapole we need to achieve the condition of Eq. 1. As shown in Fig. 3(b) the toroidal dipole reflection power T_{z} exhibits a rather weak but decent presence in the spectrum under consideration. In particular, in the spectral neighborhood of the combined TE_{000}/TE_{010}, T_{z} is featureless. However, there is a T_{z} dip at 3.55 THz which indicates that there is a significant amount of toroidal dipole within the excited TE_{200} quadrupole mode [the toroidal dipole stems from the modification of the Mie quadrupole mode of Fig. 1(c) due to the $\hat{\mathbf{z}}$-axis corrugation and the $\hat{\mathbf{y}}$-axis periodicity] and interferes destructively with the T_{z} tail of TE_{000}/TE_{010}. On the other hand, Fig. 3(b) seems to indicate that the sought after anapole could potentially be found where the reflected power from p_{z} and T_{z} cross (two positions around 2.85 THz). Nevertheless, the toroidal dipole moment is still significantly weaker than the electric one around this spectral region. A more serious obstacle is the dominance of the magnetic dipole and the electric quadrupole over the toroidal in the spectral region of interest as witnessed in Fig. 3(b). Thus, in order to achieve the anapole we need to enhance the toroidal dipole moment and eliminate the competition coming from the magnetic multipole contributions. Up to now we exploited the different size of the cross sections. Other degrees of freedom are the heights H_{S} and H_{L} of the small S and large L parts of the metaatom. In fact, the resonant frequencies of the magnetic modes

are expected, as a result of their complicated current distributions, to be much more sensitive to the heights than the uniform electric modes; this provides a strong design tool for its isolation. Thus, the strategy to strengthen the relative toroidal component is to assume a greater height H_{L}.

In this way, we can excite higher order modes in the $\hat{\mathbf{z}}$-axis direction where the current is allowed to flow reversely within a single metaatom. In particular, we have found that if we set the parameters around the values $H_{\mathrm{L}} = 40$ μm, $H_{\mathrm{S}} = 8$ μm and $R_{\mathrm{L}} = 15$ μm and $R_{\mathrm{S}} = 3$ μm for the heights and the cross-sectional radii respectively, while the periodicity is $d = 35$ μm, we do get a relevant enhancement of the toroidal moment. At these heights, $H_{\mathrm{S}} \sim \lambda_{\mathrm{n}}/2$ and $H_{\mathrm{L}} \sim 2.5\lambda_{\mathrm{n}}$ (where $\lambda_n = \lambda_0/n = 15$ μm for the central frequency of 3 THz) a drastic modification of the combined $\mathrm{TE}_{000}/\mathrm{TE}_{012}$ mode occurs: while there is no $\hat{\mathbf{z}}$-axis variation in the small cross-section part of the metaatom, a strong variation appears along the $\hat{\mathbf{z}}$-axis for the large cross-section part as the third subscript "2" indicates.

The distribution of the polarization currents for the combined $\mathrm{TE}_{000}/\mathrm{TE}_{012}$ is shown in Fig. 4(b). Figure 4(a) presents the schematic of the side-view of the metaatom. Notice that we have induced an asymmetric placement of the smaller cylinder along the $\hat{\mathbf{y}}$-axis at a position $y = 10$ μm. By introducing this asymmetry, we are able to further modify the magnetic excitations and in particular to suppress their contribution at the vicinity of the combined $\mathrm{TE}_{000}/\mathrm{TE}_{012}$ eigenmode (the electric and the toroidal modes are not affected to the same extent as the magnetic ones by this asymmetry as they do not possess azimuthal variations). Another way to tackle the magnetic quadrupole could be by assuming elliptical cross-section and increasing its spectral separation like in [30], but this did not provide an improved result. By enhancing the toroidal contribution and by eliminating the magnetic quadrupole we are able to satisfy the anapole condition of Eq. (1). Towards this goal, we also numerically optimized the geometrical parameters of the structure as follows: $H_{\mathrm{L}} = 39$ μm and $H_{\mathrm{S}} = 7.8$ μm, $R_{\mathrm{L}} = 14.625$ μm and $R_{\mathrm{S}} = 2.95$ μm and $d = 34.125$ μm. Figure 4(c) presents the reflected (by the numerically optimized metasurface) power of the multipoles. The multipoles reflection contributions present more complicated yet as expected resonant features compared with those in Fig. 3(b), as a result of the asymmetric positioning of the small cross-section cylinder. In Fig. 4(d), the overall reflection R by the metasurface is presented both by employing the direct full wave and by summing the amplitudes of all multipoles, $R = f(\mathbf{p},\mathbf{T},\mathbf{m},\mathbf{Q}^{\mathrm{m}},\mathbf{Q}^{\mathrm{e}},\mathbf{Q}^{\mathrm{T}},\mathbf{O}^{\mathrm{m}},\mathbf{O}^{\mathrm{e}})$; if in the last sum we keep only the amplitudes of the electric and the toroidal dipoles we obtain what is denoted by $R = f(\mathbf{p},\mathbf{T})$. The latter is compared with the overall reflection coefficient, leading to the conclusion that the zero reflection at the vicinity of the $\mathrm{TE}_{000}/\mathrm{TE}_{012}$ resonance ($f_{000/012} = 2.646$ THz) is due to the destructive interference of the electric and the toroidal amplitudes; this conclusion is further supported by the fact that the toroidal and electric dipole moments meet with an opposite phase (e.g. $\Delta\phi = -\pi$) at this frequency. A minor discrepancy in frequency in the order of 0.2% is observed and at the exact frequency of the anapole, a small radiation leakage of 10% coming from the reflection power contributions of all other multipoles is recorded. Thus, we have obtained beyond any doubt, the creation of an anapole by the destructive interference of

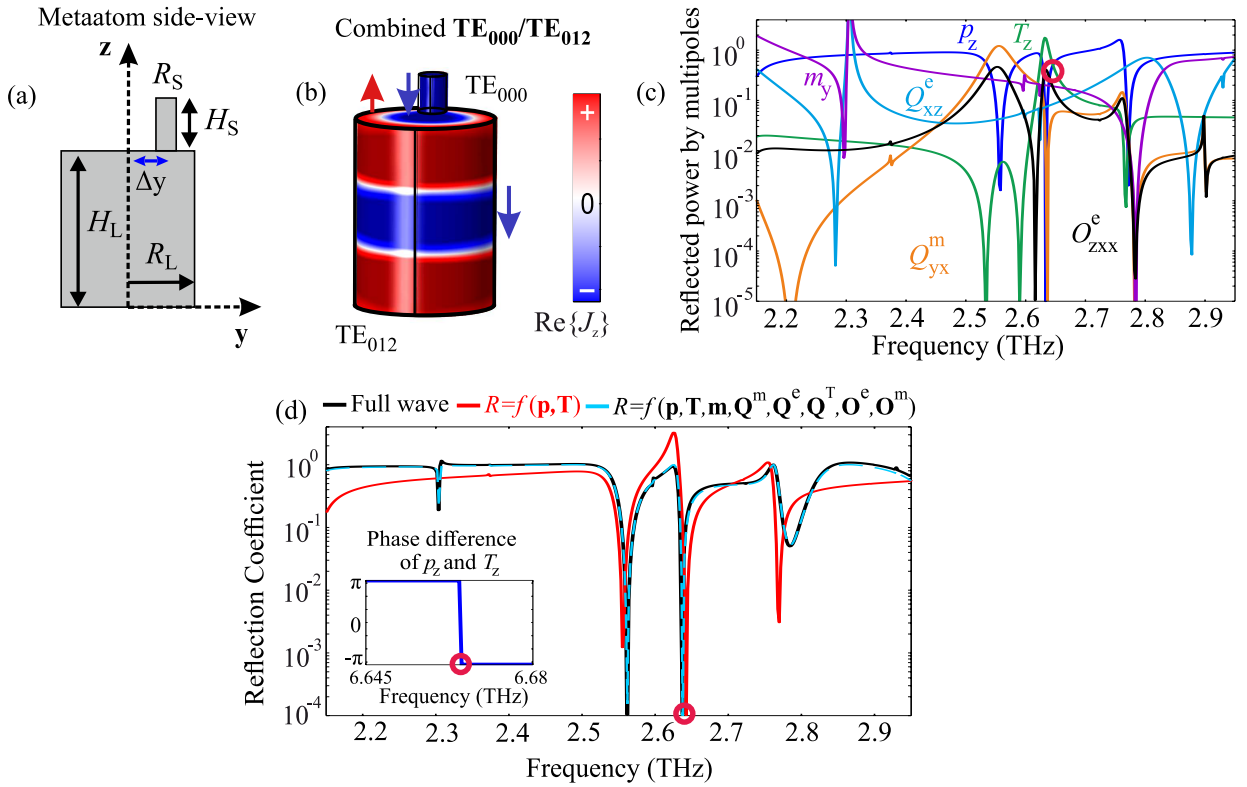

FIG. 4. (a) Schematic representation (side-view) of the unit cell with a displaced smaller cylinder. Its center is placed at $y = 10$ μm with respect to the axis of the larger cylinder. (b) Polarization current distribution of the TE_{012} mode which is characterized by the reversal of the current flows within the unit cell along the $\hat{\mathbf{z}}$-axis (the third subscript "2" denotes this reversal). The TE_{012} mode is sustained by the larger cylinder comprising the unit cell, while the small cross section sustains the TE_{000} mode. (c) Moments contribution to the reflected power, for the optimized metasurface with a unit cell as in Fig. 4(a). The combined TE_{000}/TE_{012} eigenmode of Fig. 4(b) lies at 2.646 THz and exhibits a T_z power exceeding the p_z power. (d) Total reflection coefficient (directly from the full wave, black; and by adding all amplitudes, blue) and reflection coefficient including only the electric and toroidal dipole moments amplitudes (red) for the range 2.15-2.95 THz. The red curve is almost identical to the total reflection coefficient (a small shift is due to the magnetic moments contribution) showing that the sharp dip at 2.646 THz (i.e. the appearance of anapole behavior) is indeed mainly due to the destructive interference of electric and toroidal dipoles. This is further supported by phase difference $\Delta\phi = -\pi$ between the p_z and the T_z dipoles (inset).

electric and toroidal dipole amplitudes almost without interference of any other multipole moments. This achievement was realized by our optimized metasurface composed of sculptured cylinders periodically placed along the $\hat{\mathbf{y}}$-axis; each cylinder is formed by asymmetric metaatoms [see Fig. 4(a)] periodically repeated along the $\hat{\mathbf{z}}$-axis. The circular symmetry breaking was essential in removing parasitic magnetic contributions to the anapole.

C. Metasurface sensitivity to material losses

Up to now, we have obtained the anapole excitation in the polaritonic metasurface assuming no material losses. In what follows, we examine the effect of the material losses on the anapole state. Notably, it appears that the anapole excitation in our system exhibits a considerable sensitivity to the material losses. Figure 5 presents the multipole contributions to the reflected power (top panels), as well as the overall reflection coefficient (bottom panels) for the optimized metasurface presented in Fig. 4(a) assuming a material with variable losses. The frequency range of the calculations is focused around the anapole state of the optimized structure (Fig. 4) and is equal to 2.6-2.7 THz. For the real part of the material permittivity we use the nominal value for the polaritonic $LiTaO_3$, $\epsilon_1 = 41$, and various values of fictitious losses with tangent ranging from $\tan\delta = 10^{-3}$ [Fig. 5(a)] to $\tan\delta = 9\times10^{-3}$ [Fig. 5(d)]. Low losses, with tangent in the order of few 10^{-3} have essentially little effect for the anapole realization, which is the case of the $LiTaO_3$ in the frequency range under consideration ($\tan\delta \sim 2.5\times10^{-3}$). Of course, the resonance is not as sharp and as deep as in the absence of losses. This is to be expected, since in the anapole the fields at the meta-

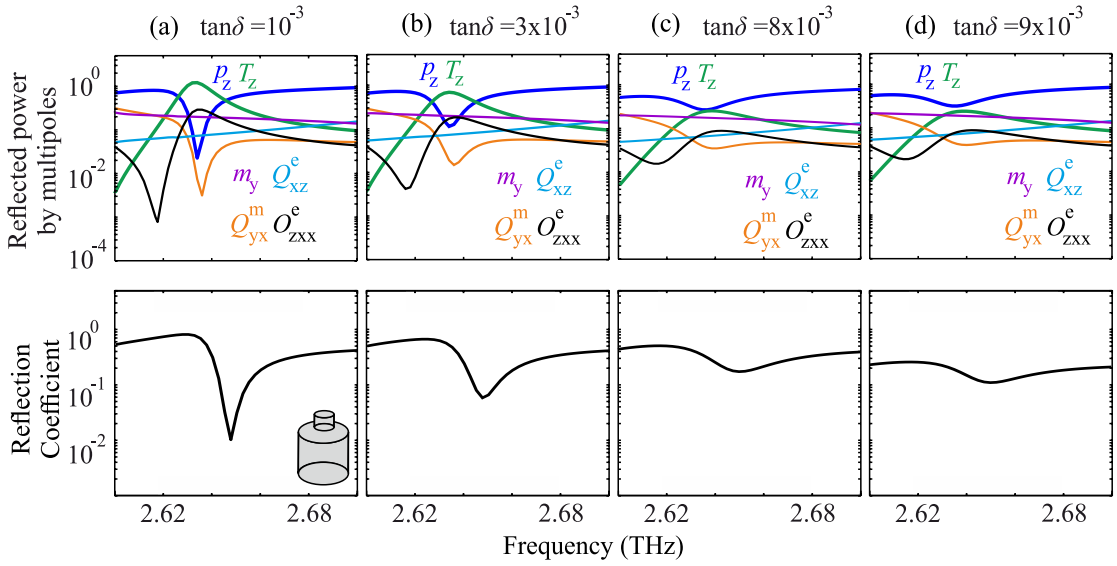

FIG. 5. Moment contributions to the reflected power, for the optimized structure of Fig. 4(a) (top panels) and total reflection (bottom panels) assuming material losses with (a) $\tan\delta = 1\times10^{-3}$, (b) $\tan\delta = 3\times10^{-3}$, (c) $\tan\delta = 8\times10^{-3}$ and (d) $\tan\delta = 9\times10^{-3}$. Above $\tan\delta \sim 8\times10^{-3}$ the electric dipole moment contribution increases extensively, it becomes dominant while the toroidal dipole moment contribution decreases and the crossings between the power reflected from p_z and T_z required for the anapole condition, seize to occur.

surface are quite strong (in spite of their absence in the far zone) and consequently there are substantial material (not radiation) losses. This behavior is evident in Fig. 5(a) and Fig. 5(b), where the calculated response of the metasurface for material with $\tan\delta = 10^{-3}$ and $\tan\delta = 3\times10^{-3}$ is shown, respectively. However, as losses increase, the crossing of the

p_z and T_z dipoles becomes borderline at $\tan\delta = 8\times10^{-3}$ [Fig. 5(c)] and beyond this value there is no crossing indicating that the condition required for the anapole is not satisfied anymore. As a result, the tendency of disappearance of the broad anapole dip is due to both material and radiation losses. In the regime beyond $\tan\delta = 8\times10^{-3}$ the electric dipole moment contribution becomes more dominant, while the toroidal dipole moment contribution diminishes. We note here that similar effect would be observed in a medium with presumable gain (not shown here), where an uneven increase of the electric dipole (dominant) and the toroidal dipole tends to eliminate the crossing of the reflected power from p_z and T_z and consequently the existence of anapole.

D. Anapole attained by hybrids of mixed electric and toroidal dipole modes

Apart from the exploitation of the fundamental electric dipole and mixed toroidal dipole mode, the binary metaatom offers the possibility to explore an anapole excitation generated by the contribution of higher and hybrid modes that entail toroidal dipole moments. This could for example be explored in the spectral vicinity of the TE_{200} resonance at 3.6 THz [Fig. 3(a)]. This resonance includes a significant but hidden presence of toroidal dipole moment T_z simultaneously with the magnetic quadrupole Q^m_{yx} and the other multipoles. By breaking the symmetry of the metaatom this hidden toroidal character is revealed and isolated from the quadrupole and other contributions offering an effective tool towards realization of the anapole. In Ref. [30], it has been shown that this can be accomplished by introducing elliptical cross-sections in the metaatoms. In the present case, we further break the circular symmetry by introducing an additional perforation in the large cross-section of the metaatom of Fig. 4.

We apply this off-center perforation to a *uniform* cylinder as shown in Fig. 6(a). Splitings in the eigenfrequencies and changes in the current distributions are produced; the latter may be as serious as to drastically modify the character of the eigenmodes [see the TE_{20} case in Fig. 6(a)] and their multipole components [Fig. 6(b)]. As mentioned before, the perforation greatly affects the magnetic type modes, causing their distinctive splitting in frequency, and has minor effect on the electric type modes. We observe this in Fig. 6; the perforated cylinder supports the fundamental TE_{00} mode, two splitted magnetic dipole modes with $\hat{\mathbf{x}}$-axis and $\hat{\mathbf{y}}$-axis orientation TE^x_{10} and TE^y_{10}, the fundamental mixed toroidal TE_{01} mode and two splitted magnetic quadrupole modes $TE^{(1)}_{20}$ and $TE^{(2)}_{20}$. The expected radiation contributions (calculated as in Fig. 1) presented in Fig. 6(b) provide further insight in the electromagnetic character of each mode. Here we choose to discuss only the above mentioned since they are the significant ones for our purposes. (For example, mode TE^x_{10} has a dominant m_x contribution that will not be excited). What is interesting is that the splitted quadrupole mode $TE^{(2)}_{20}$ has a significant T_z contribution with respect to the non-splitted TE_{20} mode seen in Fig. 1. This is the feature we plan to exploit in the present approach, since the features of the perforated single infinite uniform cylinder presented in Fig. 6 survive in the perforated large part of the metaatom [see Fig. 7(a)], the unit cell of the

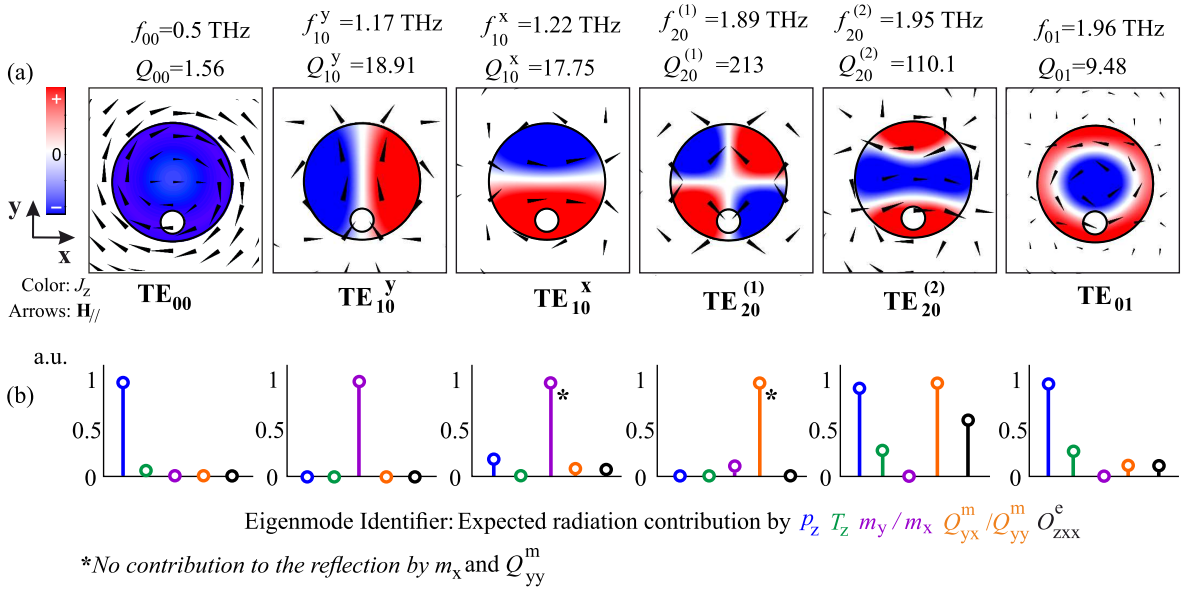

FIG. 6. (a) First six transverse electric eigenmodes of a single infinite length uniform polaritonic rod with a circular perforation; current distribution (color), resonant frequency, quality factor, and magnetic field lines (arrows) are shown. We assume E_z polarization and eigensolutions whose wavevector remains strictly in the xy plane, $k_z = 0$. The radius of the cylinder is $R_c = 15$ μm and the radius or the perforation $r_p = 3$ μm placed at $y = -10$ μm. The sustained modes are the electric dipole, TE_{00}, two splitted magnetic dipoles, TE_{10}^{y} and TE_{10}^{x}, two splitted magnetic quadrupoles $TE_{20}^{(1)}$ and $TE_{20}^{(2)}$ and the mixed electric and toroidal dipole, TE_{01}. Notice that the expected radiation corresponding to the $TE_{20}^{(2)}$ mode has been dynamically altered by the perforation compared to the TE_{20} eigenmode of Fig. 1(b). (b) Eigenmode identifier with respect to the expected radiation contributions coming from the electric dipole p_z, the toroidal dipole T_z, the magnetic dipole m_y, magnetic quadrupole Q_{yx}^{m} and the electric octupole O_{zxx}^{e}. The radiation power contributions are normalized with the dominant one in each mode individually.

sculptured cylinder. The perforation is a vertical circular hole placed at the symmetric position ($y = -10$ μm) of the small off-center cross-section part and with the same radius. Note that all the features depend on the size of the perforation which we here keep constant. The new design of the metaatom involves the $TE_{20}^{(2)}$ hybrid quadrupole mode of the perforated cylinder, entailing electric and toroidal dipole moments with a pure electric dipole sustained by the small-cross section part of the metaatom. The parameters are set at $H_L = 40$ μm and $H_S = 8$ μm for the cross-sectional lengths, $R_L = 15$ μm and $R_S = r_p = 3$ μm for the cross-sectional radii and the radius of the hole. The cylinders are periodically arranged with the $\hat{\mathbf{y}}$-axis periodicity being equal to $d = 40$ μm. Fig. 7(c) presents the reflection response of the metasurface and in the inset of Fig. 7(c) we present the power contribution of the various multipoles to the reflected power. The contribution from the toroidal dipole peaks at ~2.56 THz where the electric dipole exhibits a dip. The p_z and T_z power contributions cross at two points, one of which produces a dip in the reflection, satisfying the anapole condition

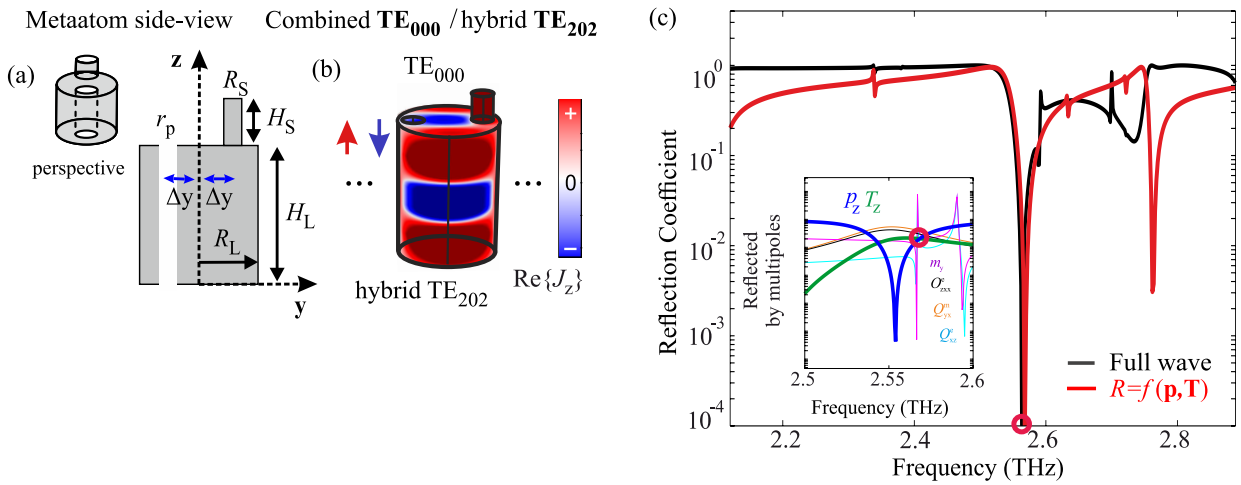

FIG. 7. (a) Schematic view of the perforated metaatom including the off-center small cross-section part ($r_p = R_S$). The corresponding metasurface sustains a dynamic anapole generated by the cancellation of the p_z and T_z moments; the latter originates from quadrupole Mie mode split as a result of breaking of the circular symmetry. (b) The distribution of the polarization currents of the hybrid quadrupole mode that entails, amongst else, enhanced toroidal dipole moment T_z (c) Reflection coefficient, assuming E_z polarization and normal incidence, calculated by full wave analysis (black) and as interference of the reflected amplitudes of only the p_z and T_z dipoles (red); in the inset the reflected power by several multipoles is shown.

of Eq. (1). This is also evident by the fact that the anapole dip almost coincides with the dip produced by the interference of only the p_z and T_z contributions, $R = f(\mathbf{p},\mathbf{T})$ (red), although there are at this frequency strong magnetic dipole and quadrupole and electric octupole moments [see Fig. 7(c), inset], which apparently cancel each other out. The quite minor discrepancy in the position of the $R = f(\mathbf{p},\mathbf{T})$ and the total reflection dip is $\Delta f/f_0 = 0.1\%$, while in this case a very small leakage in the order of 1% is recorded in the reflection (calculated by the full wave analysis). Thus, we have obtained beyond any doubt, the creation of an anapole by the destructive interference of electric and toroidal dipole amplitudes almost without interference of any other multipole. This achievement was realized by our optimized metasurface composed of sculptured cylinders periodically placed along the $\hat{\mathbf{y}}$-axis; each cylinder is formed by metaatoms [see Figs 4(a) and 7(a)] serving as unit cells; the breaking of the circular symmetry was critical in eliminating parasitic contributions detrimental to both the existence and the nature of the anapole.

At the same time, the combination of the hybrid mixed toroidal and electric dipole modes of Fig. 7(a) proves to be more resilient to material losses than those of Fig. 4(a). This is presented in Fig. 8, where the response of Fig. 7(a) metasurface around the anapole frequency range, 2.5-2.7 THz, is calculated for a material with variable loss tangent, $\tan\delta = 5\times10^{-3}$ [Fig. 8(a)] and $\tan\delta = 10\times10^{-3}$ [Fig. 8(b)]. Top panels present the power contributions of the variable multipoles to the reflection power and bottom panels present the full wave calculated reflection. We observe that as material losses increase, the Q factors of the re-

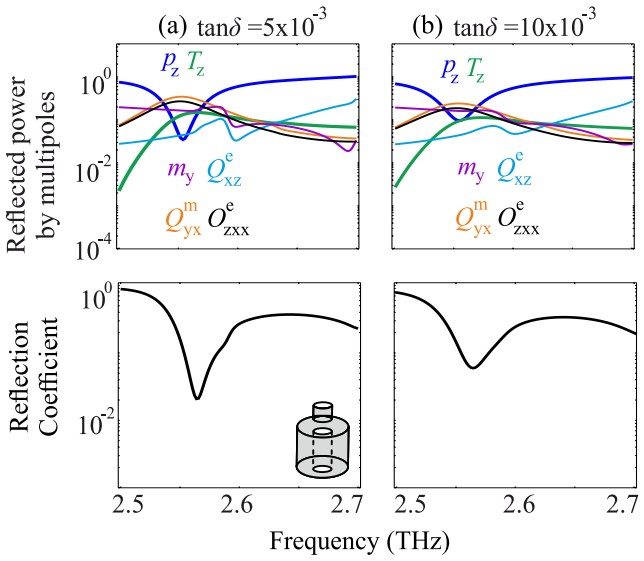

FIG. 8. Top panels: multipole contributions to the reflected power, for the optimized structure of Fig. 7(a); bottom panels: total reflection assuming material losses with (a) $\tan\delta = 5 \times 10^{-3}$ and (b) $\tan\delta = 10 \times 10^{-3}$. The electric dipole moment contribution increases extensively above $\tan\delta = 10 \times 10^{-3}$ becoming dominant, while the toroidal dipole moment contribution decreases and the crossings between the power reflected from p_z and T_z required for the anapole condition, seize to occur.

sponses decrease, leading to less sharp resonances. Additionally, the electric dipole moment contribution increases while the toroidal dipole moment contribution decreases. The crossings between the contribution reflected from the electric dipole p_z and toroidal dipole T_z remain up to the loss tangent of $\tan\delta = 10 \times 10^{-3}$ [Fig. 8(b)]. For even greater losses, the electric dipole moment contribution becomes dominant, while the toroidal dipole moment contribution vanishes.

E. Conclusions

We presented the design principle, the optimized specifications, and the simulation results of all-dielectric, polaritonic metasurfaces, consisting of sculptured periodically arranged cylinders that sustain non-radiating alternating current distributions, i.e. the so called dynamic anapole state. The sculptured cylinders are formed by the periodic repetition of a metaatom breaking the circular symmetry and serving as their building block; two different designs of the metaatom were presented based on different origins for the toroidal dipole. We show that the anapole emerges from the destructive interference of only two properly modified (as a result of the circular symmetry breaking) multipole moments: the origin of the first is mainly the TE_{00} electric dipole Mie mode and the origin of the second is either the mixed toroidal dipole Mie mode TE_{01} or the split magnetic quadrupole Mie mode, TE_{20}; the notations TE_{00}, TE_{01}, and TE_{20} are those found in an infinite, uniform free-space standing cylinder. It was proven that the breaking of the circular symmetry can effectively

eliminate the persistent magnetic contributions from the frequency of interest and allow thus the almost pure cancellation by destructive interference of the electric and toroidal dipole radiation leading to the anapole state. In the case that the toroidal dipole moment originates from the splitting of TE_{20} mode, an additional symmetry breaking perforation in each metaatom enhances the performance with respect to the anapole realization. Both designs of the metaatom have been evaluated regarding the anapole sensitivity to material dissipation losses proving to be reasonably resilient for actual implementations. Notice that the designed metasurfaces can be realized using established fabrication techniques such as direct laser writing.

III. MANY-ROD CONFIGURATIONS - WATER-BASED METASURFACES

A. Many-rod configurations

Until now, the focus was placed on the TE_{01} mixed toroidal mode (and also on a hybrid magnetic quadrupole mode) as the basic candidates from which the toroidal moment originates and is manipulated accordingly so as to achieve the anapole state. Another way to create strong toroidal moment is by combining many magnetic dipole modes (the second in ascending frequency in Fig. 1(a), TE_{10} eigenmode) in a unit cell configuration comprised of many rods. The TE_{10} eigenmode thus, becomes the building block of what is denoted as *collective toroidal super-mode*, and already has been reported previously in [31]. In fact, other electromagnetic types of collective super-modes emerge from the combination of many "meta-atoms" cylinders to form a many-rod unit cell; the electromagnetic character is affected by the interactions amongst the constituents and can be retrieved via a calculation of the moments for each of the sustainable collective eigenmodes. One distinctive feature of the collective toroidal super-mode is the pattern of the magnetic field lines. In particularly, the magnetic moments arrange themselves into a circular loop that threads all the current distributions, as shown in Fig. 9.

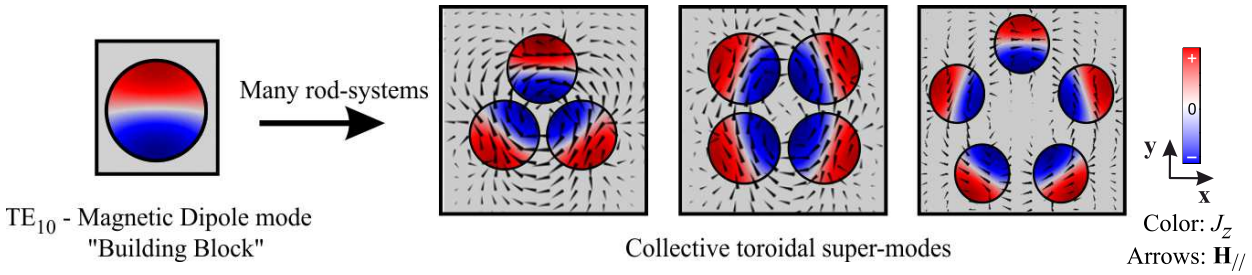

FIG. 9. The basis of the collective toroidal super-mode in many-rod systems is the fundamental magnetic dipole eigenmode of a single infinite uniform cylinder (TE_{10}). From the single-rod unit cell, unit cells of many-rods configured in canonical polygons are capable of effectively recreating the toroidal pattern; the latter is witnessed by the orientation of the magnetic moments into a circular loop which threads all current distributions of the meta-atoms.

A calculation of the toroidal moment at the eigenfrequency of the collective toroidal super-mode, reveals that adding more cylinders in the unit cell enhances the toroidal dipole character of the respective super-mode. Thus, it would be deduced that this tendency easily leads to a favourable situation to obtain an anapole state. Nevertheless, regarding the spectral isolation of the toroidal super-mode in many-rod metasurfaces, the increased number of unit cell constituents, deteriorates the spectral separation from neighbouring magnetic type super-modes. The eigenvalue analysis was also in accordance with the scattered field study. In the latter, it was observed that in the vicinity of the excited toroidal super-mode, except for the toroidal reflection power, other multipoles participated substantially to the reflection when more rods were considered; this posed problems to the realization of a potential anapole state. On the other hand, more rods in the unit cell lead to advantageous features as well, such as improved tolerance to dissipation losses alongside with the enhanced toroidal moment. Thus, a balanced result should be targeted that allows both the beneficial effects to emerge, and also restricts the problem of spectral inseparability. This was achieved for $N = 5$ rods in the unit cell; for six rods or greater, the improvement of the toroidal moment is saturated, while the spectral inseparability is intensified. Thus, this makes any effort to suppress the magnetic type contributions to the reflection rather difficult in order to create a pure anapole state.

In subsequence, structures of four and then five water-based cylinders are considered, in order to examine the response of the anapole state in the presence of dissipation losses originating from water; this is also a convenient scheme for an experimental implementation.

B. Water properties and theoretical examination of water-based metasurfaces

Water is one of the most abundant and inexpensive materials on Earth, with an advantage over rare and expensive materials such as $LiTaO_3$ (Lithium Titanate) or $Ba_xSr_{1-x}TiO_3$ (Barium Strontium Titanate). Its ability to take the size of its container and the fact that it is volume preserving, alongside with its dielectric properties, renders it a pioneer candidate in the engineering of varying-sized water-based configurations. The real part of the permittivity of pure water at room temperature is relatively high $\Re(\epsilon_r) \approx 80$, however it is also fairly lossy, especially when water contains impurity ions; this explains why water has been neglected in the design of all-dielectric electromagnetic structures, while recently novel and bold steps have been made towards its use in a variety of applications.

The complex dielectric function of water in the low GHz regime is linked to the collective motion of the molecular dipole moments under the influence of an electric field. It displays a temperature dependent dispersive profile which is given by the Debye formula [44, 45]:

$$\epsilon(\omega, T) = \epsilon_\infty(T) + \frac{\epsilon_0(T) - \epsilon_\infty(T)}{1 - i\omega\tau(T)} \tag{5}$$

where ω is the angular frequency, $\epsilon_0(T)$ is the static permittivity (expressing the response of the material when exposed to a static field), $\epsilon_\infty(T)$ is the permittivity at a higher frequency

beyond the electronic transitions and τ is the rotational relaxation time. The temperature dependence of the dielectric function is useful for the optimization of the performance of water-based metasurfaces. In Appendix IV B, the exact relations for ϵ_∞, ϵ_0 and τ of Eq. (5) are provided.

In liquid water, the molecules are linked together via a disordered network of hydrogen bonds. Each hydrogen atom of one molecule is attracted to the oxygen atom of another molecule that is located within a distance of few angstroms. Reorientation refers to the process that occurs when a water molecule breaks a hydrogen bond and then reforms with another molecule. Up to ~100 GHz the spectrum of water is dominated by this re-orientational contribution. In Fig. 10 the real (ϵ') and imaginary (ϵ'') parts of the water permittivity are depicted and reorientation is labelled with R. The three bands at higher frequencies are denoted by B, S and L and refer to the bending and stretching (both of which belong to the intermolecular vibrational modes) and librational motion of molecules about their centres of mass [46].

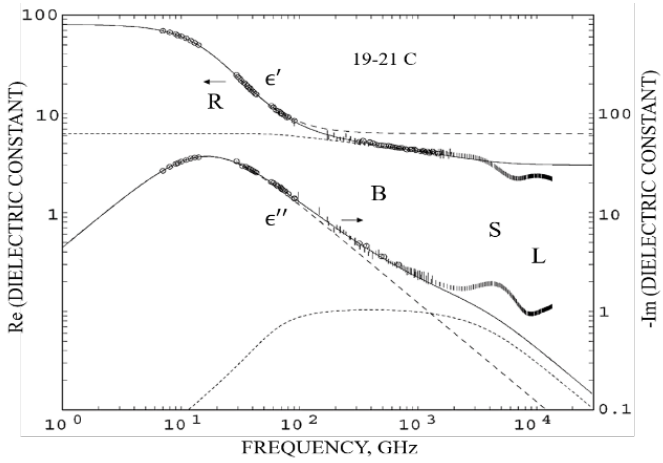

FIG. 10. Complex permittivity of water as a function of the frequency. The lower frequency behavior is accounted for by the reorientation (R) of the water molecules [46].

To test the dielectric properties of water and examine its role when it is implemented in a metasurface, a design to retain the water needs to be introduced. Such a design should be described by repeated containers, into which water can be incorporated and they should have a simple enough geometry convenient for construction processes. One of the simplest schemes could be cylindrical glass containers that can be filled with water. Since glass is a material whose relative permittivity is to the order $\epsilon_r = 2 - 10$, whereas the water permittivity highly exceeds this values, an impinging wave is only affected by the electromagnetic properties of water and not those of glass.

Therefore, the theoretical study for the anapole state in water-based metasurfaces begins by considering water-based cylinders. For $T = 20^o$, the permittivity preserves a significant real value of $\Re(\epsilon_r) \sim 80$ and displays a relatively low imaginary part to the order of $\Im(\epsilon_r) \sim 4.46 - 13$ for frequencies 1 to 3 GHz. The loss-tangent in this case ranges from $\tan\delta =$

0.056 for $f = 1$ GHz, to $\tan\delta = 0.167$ for $f = 3$ GHz at room temperature. Both the real and imaginary parts of the dielectric function are decreasing, as the temperature of the water increases. In fact, the loss-tangent as well, is a decreasing function of temperature and therefore the dissipations are lower if heated water is considered. The reason for the tendency of the loss factor to be shifted to higher frequencies is explained more thoroughly in Appendix IV B.

In Fig. 11(a) the real and imaginary part of water permittivity is presented and in Fig.11(b) the loss-tangent. In order to restrict the dissipation losses to low values, the frequency range below 2 GHz was studied, where the re-orientational process of water is responsible for its dielectric properties.

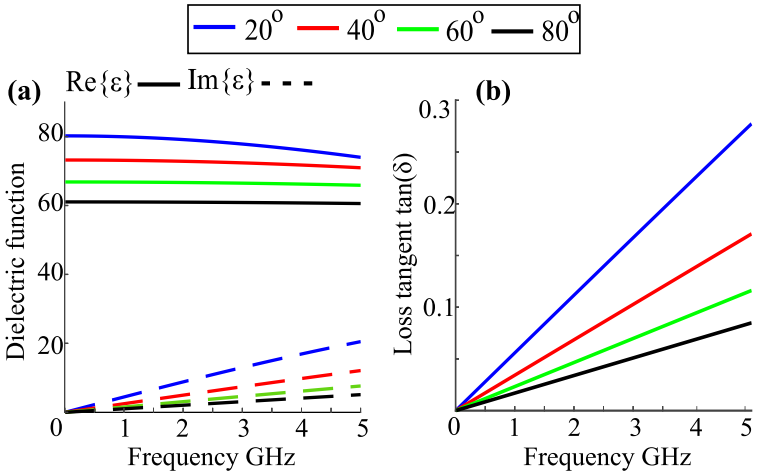

FIG. 11. (a) Temperature and frequency dependent profile of the dielectric function of water based on Eq. (5), up to 5 GHz. Color-coded solid lines correspond to the real part of the permittivity and dashed to the imaginary. (b) Loss-tangent as a function of frequency and water temperature.

As introduced in Sec. III A, the "conventional" many rod-configurations, could potentially be manipulated so as to sustain an anapole state, due to the enhanced toroidal moment originating from the excitation of the collective toroidal super-mode. The first system to be examined theoretically, combining the water-based and the many-rod design, is that of four water-filled uniform cylinders placed on the edges of a rectangle, and repeated periodically so as to form a metasurface. This structure has already been discussed in [47, 48], in the first one theoretically (not for water-based system thought) and in the second one both theoretically and experimentally as a water-based structure with no temperature tunability. Here, it will be proven that the high dissipation losses at room temperature do not enable the emergence of a pure anapole state in the four-rod metasurface. An analysis of the reflection power of each moment as well as the evaluation of the reflection and transmission coefficients, reveals that there are many obstacles that need to be overcome. First of all, the toroidal reflection power in frequencies close to the excited collective toroidal super-mode, is severely weakened by the dissipation losses; these reach even 70% (at room temperature), and especially above 2 GHz the situation is deteriorated. Therefore, the T_z reflection power

is significantly lower than the p_z power above 2 GHz. As a result of the high percentage of losses, the expected transmission power (it would be equal to one in the ideal lossless case at the excitation frequency of the anapole state) is also severely decreased. Thus, careful inspection of all the available many-rod configurations needs to be employed and the frequency range should be restricted below 2 GHz for lower dissipation. The most advantageous number of cylinders to be used in the unit cell of the metasurface so as to accommodate the anapole state is claimed to be $N = 5$. Indeed, this conclusion stemmed from an extensive analysis of water-based metasurfaces composed of $N = 3$ until $N = 9$ unit cell constituents. Those results are not presented in this thesis, but were used to determine the most beneficial configuration.

The two systems chosen to be presented (four- and five-rod configurations), display the distinctive differences and summarize the major changes that occur when the number of the water-based cylinders within the unit cell of a metasurface is altered. To perform the comparison amongst them, the period of adjacent unit cells is set to 109.2 mm and the diameter of the cylinders to 16.1 mm. Also, a constant center-to-center adjacent rod separation of 26 mm is considered. In this way, a "fair" comparison of the temperature effects on the transmission and on the absorption losses, regarding each configuration, can be made. As expected, the water temperature rise improves both the toroidal reflection power and the transmission near the excitation of the collective toroidal super-mode, while the resonance is shifted to a higher frequency. This stems from the fact that the water permittivity decreases with temperature [see Fig. 11(a)], thus the wavelength also decreases, and as a result the frequency is shifted to a higher value.

For the four-rod system [cylinders positioned as illustrated in Fig. 12(a)], the transmission curves are depicted for varying temperatures as a function of frequencies that lie below 2 GHz [Fig. 12(b)]. A step of 10^o temperature increase improves the maximum transmission attained near the collective toroidal resonance by $\sim 5\%$. The excitation of the collective toroidal super-mode occurs at the first maximum in the transmission power of Fig. 12(b) of each temperature case. If additionally the reflection powers of the electric and toroidal moments are examined, it is concluded that the threshold temperature for a crossing-point to exist is above 80^o, as it is shown in Fig. 12(c). Thus, this structure is heavily affected by the dissipation losses. An enhancement is observed to the power of T_z if the center-to-center separation is increased, but this leads to a deterioration in the transmission and to a persisting magnetic quadrupole (and magnetic dipole) reflection contribution to the vicinity of the excitation of the toroidal super-mode. These additional contributions are also evident in this case, by the fact that $R = f(\mathbf{p}, \mathbf{T})$ fails to reproduce the total reflection power, as shown in Fig. 12(d).

Since the four-rod water-based configuration does not offer a broad temperature and frequency range to be exploited for the realization of a potential anapole state, the attention is turned to the five-rod system. As already stated, the $N = 5$ number of rods was the most beneficial case, since it combined both decent spectral isolation of the collective toroidal excitation, as well as significant toroidal dipole contribution. For the five-rod system [ar-

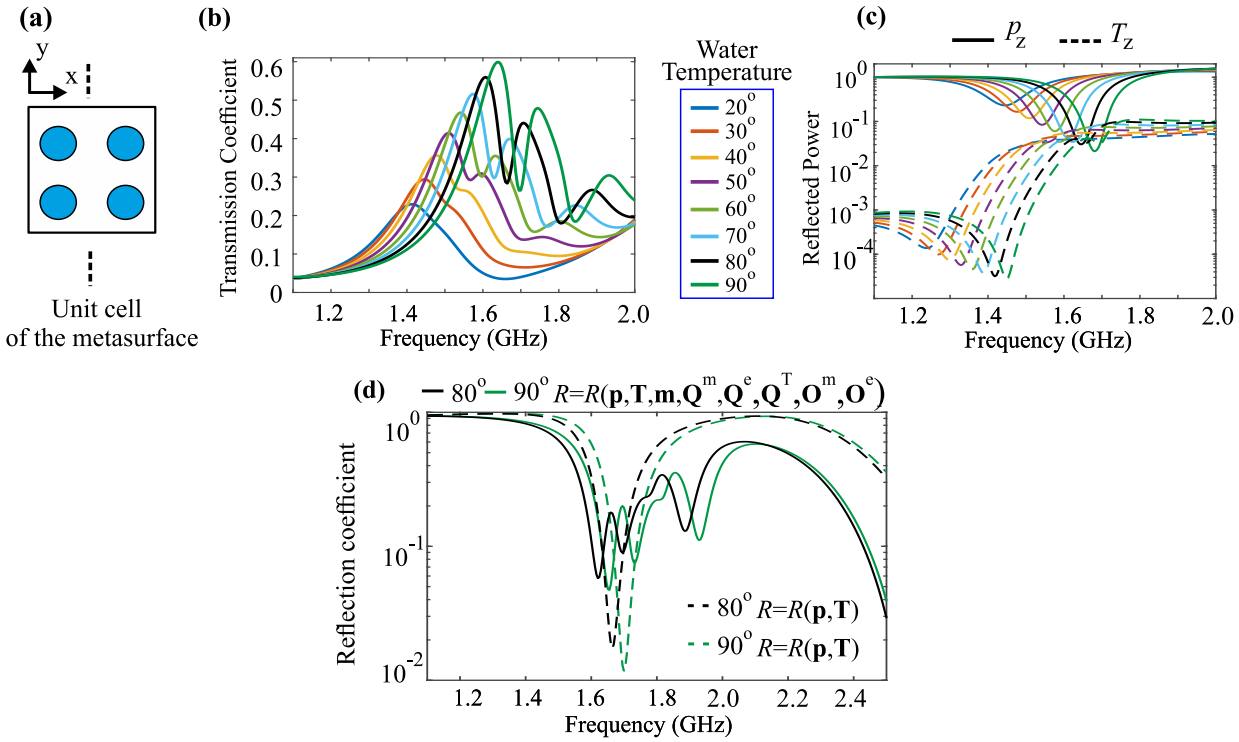

FIG. 12. (a) Unit cell of the four-rod water-based metasurface. (b) Transmission power as a function of the frequency for water temperatures ranging from 20^o to 90^o, for 1.1-2 GHz. The peak value in each temperature occurs at the excitation of the collective toroidal super-mode. (b) Reflection power from p_z (solid) and T_z (dashed) for the same frequency range as in (a). The threshold temperature to preserve the crossing of the two reflection powers is approximately 80^o. Below this threshold, due to the dissipation losses the toroidal moment fails to reach a power comparable to the electric dipole. (d) Reflection power as a function of all multipoles (solid) and of only the toroidal and electric dipolez $R = R(\mathbf{p},\mathbf{T})$ (dashed) in the range 1.1-2.5 GHz, for the two temperature cases of lowest dissipation losses. Notice the discrepancy between the total reflection coefficient and $R = R(\mathbf{p},\mathbf{T})$; the latter is both shifted and of lower amplitude, indicating extra contribution that needs to be considered and originates from the m_y, Q^e_{xz} and Q^m_{yx} reflection powers.

ranged in a pentagon as shown in Fig. 13(a)], the threshold temperature for the crossing to occur is approximately 65^o.

Again, for each temperature the corresponding transmission is demonstrated [see Fig. 13(b)]. It is observed that this configuration is more tolerant to dissipation and the maximum transmission in this case is about $60-65\%$ for $T = 90^o$. In addition, it offers better spectral separability from the collective magnetic quadrupole excitation. The anapole state corresponds to the sharpest peak observed in Fig. 13(b), and the reflected powers from p_z and T_z are depicted in Fig. 13(c). In this case, the temperature range in which the anapole state is resilient and still sustainable in the presence of losses, increases significantly by $\sim 25^o$ compared to the four-rod water-based metasurface. Furthermore, the comparison of

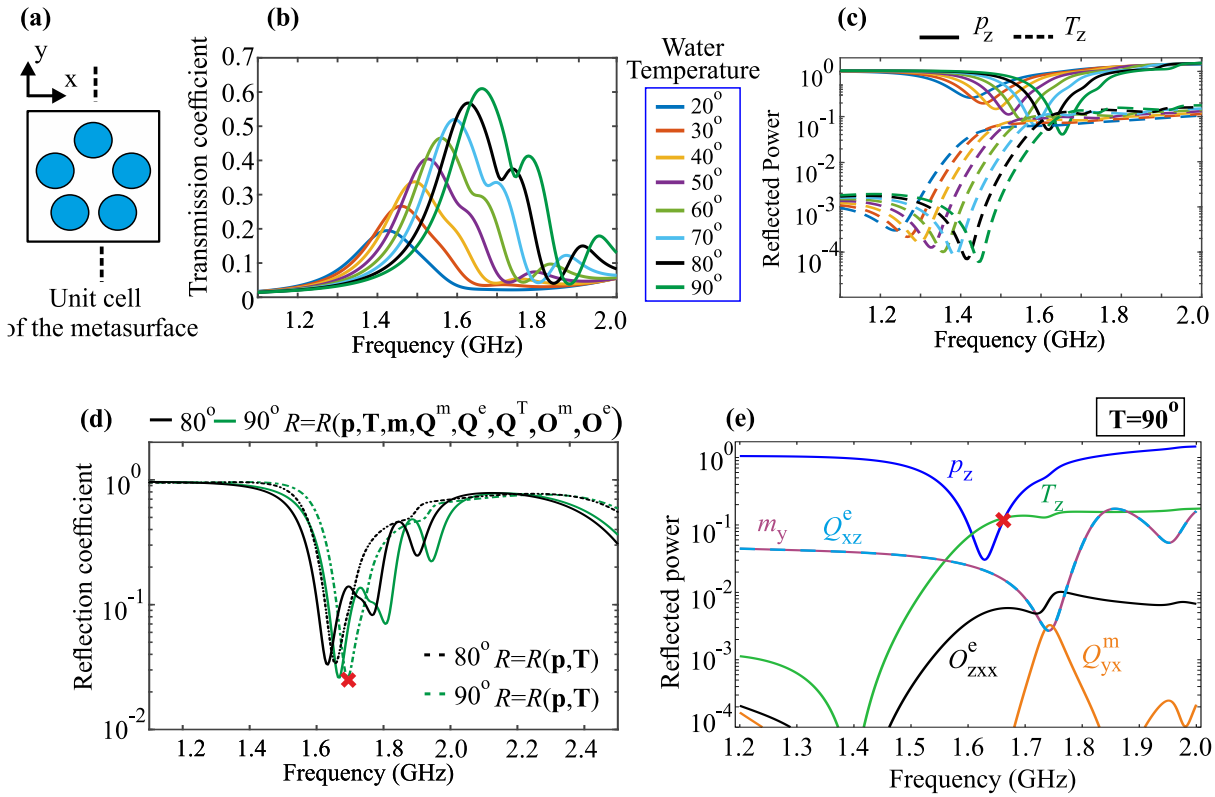

FIG. 13. (a) Unit cell of the five-rod water-based metasurface. (b) Transmission coefficient as a function of the frequency for water temperatures ranging from 20^o to 90^o. (c) Reflection power from p_z (solid) and T_z (dashed) for different temperatures. Above $55^o - 60^o$ the crossing of the two reflection powers is observed, offering wider potential for operation than the corresponding four-rod system. (d) Reflection coefficient as a function of all multipoles and of only the toroidal and electric dipole $R = R(\mathbf{p},\mathbf{T})$ in the range 1.1-2.5 GHz, for the two cases of lowest dissipation losses. Increase of the temperature results in a sharper reflection dip and the anapole state occurs at ~1.6 GHz, with a $\delta f/f_0 \sim 1.3\%$ for 80^o and $\delta f/f_0 \sim 1.2\%$ for 90^o, regarding the comparison between the total reflection and $R = R(\mathbf{p},\mathbf{T})$. (e) Reflected power by multipoles for 1.2-2 GHz. The crossing point (indicated with "x") of the p_z and T_z powers corresponds to the minimum of the reflection coefficient in (d).

the total reflection power with the reflection when only the toroidal and electric dipole moments are considered is much more accurate; the minor shift is only ~0.02 GHz [see Fig. 13(d)]. Finally, in Fig. 13(e) the reflected power by the individual moments is displayed. The anapole state occurs at ~1.65 GHz and it is also shown that only a negligible contribution by the m_y and Q^e_{xz} powers contributes. Thus, this metasurface prominently succeeds in attaining the long-sought dynamic anapole state by simply exploiting the most abundant material in nature, the water.

The general conclusion is that if one follows the same procedure by adding one more rod to the unit-cell, the toroidal reflection power is enhanced. Consequently, the temperature threshold needed to be reached so as to sustain the anapole decreases by approximately

$\sim 10^o$, when the number of cylinders increases by one. Nevertheless, for $N \geqslant 6$ there is no distinct improvement to the maximum transmission (and equivalently minimum reflection), since the losses become more intense due to the increased occupied volume area of the material within the unit cell (filling factor), whilst additional magnetic type contributions at the vicinity of the cannot be suppressed.

C. Waveguide experiment using water-filled cylinders

In order to test the theoretical results, an experiment was performed in one of the laboratories of Forth IESL, by utilizing five water-filled glass cylinders. The relative permittivity of the glass containers was $\epsilon_r = 4$ and their width 2 mm. The inner region of the cylinders was 16.1 mm and was filled with deionized water. The five cylinders were adjusted to an adjacent center-to-center separation of 26 mm (in accordance with the theoretical analysis in Sec. III B), and fixed onto a glass substrate as in Fig. 14(a).

FIG. 14. Experimental configuration of the five-rod unit cell. Five cylinders filled with deionized water, forming a canonical pentagon, were adjusted onto a circular glass base.

The unit cell of Fig. 14 was then inserted inside a metallic waveguide, 10.9 cm wide. The width of the waveguide is critical, and it must be at least $\lambda/2$ to accommodate a quarter-wave stub on each side and still have nonvanishing conductor strips. This means that there exists a low-frequency cutoff; wave propagation is not possible if the wavelength is greater than $2a$, where a is the waveguide width. The one used in the experiment is the standard design WR430 (Fig. 15), meaning "Waveguide Rectangular", and is 4.3 inches (10.9 cm) wide. The standard width-to-height ratio is two-to-one, so the height of the waveguide is 54.61 mm [49]. The transverse electric waveguide modes are denoted as $\mathrm{TE_{mn}}$, where the integers m and n indicate the number of half wavelength or nodal lines which the interference wave possesses in the rectangular cross-section. The cutoff frequency of lowest order transverse electric mode ($\mathrm{TE_{10}}$) for this type of waveguide is 1.372 GHz, and for the next mode ($\mathrm{TE_{20}}$) 2.745 GHZ. Thus, it is now apparent why in the previous section the anapole state was aimed to be obtained at frequencies exceeding 1.3 GHz, and why the periodicity was set to 109.2 mm. Placing a unit-cell within a waveguide of a certain width, is in quality equivalent to an infinite metasurface of repeated unit-cells, due to the boundary conditions at the

metallic walls, that in the low GHz regime for the fundamental waveguide mode mimic the periodic boundary conditions of the **E** and **B** fields. The infinite elongation along the axis of the cylinders (which applies to the case of the metasurface) is again equivalent with cylinders filling exactly the height of the waveguide.

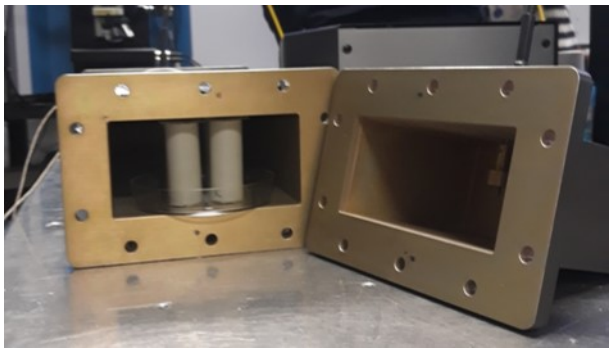

FIG. 15. A WR430 waveguide was used and the five-rod configuration was placed within the waveguide. The lowest cutoff frequency of the fundamental TE_{10} mode is 1.372 GHz. The width of the WR430 is 109.22 mm and the height 54.61 mm. These values refer to the inner dimensions of the opening of the waveguide.

As stated, inserting one unit-cell within the waveguide is expected to reproduce closely enough the conditions of an infinite metasurface with period of adjacent unit cells equivalent to the width of the waveguide. As far as the height of the cylinders, they were a little shorter than the height of the waveguide, so that they could be easily inserted and removed from the waveguide. The fundamental mode of the waveguide, that is the TE_{10} mode, is the one that resembles as closely as possible the TEM wave (plane wave that impinges on a metasurface). It is known that a waveguide cannot support a TEM wave. The TEM wave is different from the TE_{10} in a sense that every wavefront of the former has constant spatial amplitude and a specific polarization. The TE_{10} also has a specific constant polarization direction on each cross-section of the waveguide; however, there is a sinusoidal dependence of the amplitude on the x, y coordinates in every cross-section (assuming propagation along the $\hat{\mathbf{z}}$-axis parallel to the length of the waveguide), but since only $\lambda/2$ fit in the waveguide for this mode, each wavefront retains a constant direction of polarization within the two-node envelope. This is the main difference between a TEM wave and the TE_{10} mode of the waveguide, and the latter is the closest equivalence with a plane wave that could be obtained with this experiment. Therefore, the expectations are that the theoretical results of Sec. III B, for a plane wave impacting on the infinite metasurface, will exhibit some discrepancy with the experimental ones.

Each side of the waveguide has two probes; the one is used to generate electromagnetic waves that couple to the modes of the waveguide and propagate along its length, and the second is used to record the signal related to the phase and amplitude of the transmission coefficient S_{21}. Also, the two opposite sides of of the waveguide have one quarter-wave impedance transformer each, specially designed so as to avoid power being reflected back

to the input port, when the waveguide is empty. This feature is wanted in order not to send radiation back to the unit cell from the second end.

Within most of the recorded frequency range of this experiment, only the fundamental TE_{10} was propagated along the waveguide. As it was emphasized in Sec. III B, control over the temperature of the water is wanted, but a waveguide itself does not possess a heating mechanism. To further allow temperature control, a heating belt [see Fig. 16(a)] was wrapped around the waveguide directly above the location of the unit-cell. Since the waveguide is metallic, it allows heat to permeate in the inner region, warming thus the water that fills the cylinders. To prevent extensive heat loss, both the waveguide and the belt are wrapped with an aluminum foil as shown in Fig.16(b). The temperature could then be varied, and was measured via a sensor that was connected to the inner region of the waveguide. All data regarding the transmission and reflection coefficients were collected by means of a digital analyser [see Fig. 16(c)].

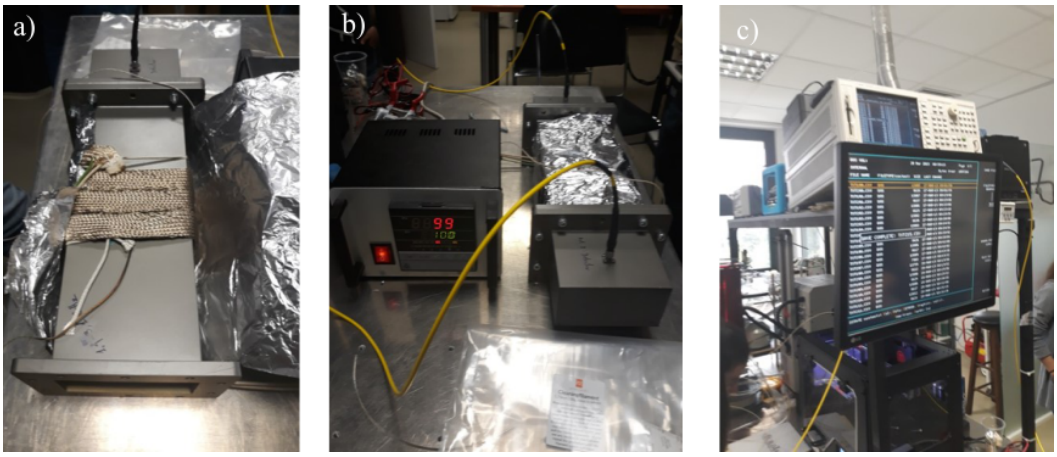

FIG. 16. (a) Heating belt wrapped around the waveguide to provide control over the temperature of the water within the cylinders. The heat flows from the outer to the inner part of the waveguide. (b) The waveguide is covered with aluminum foil for extra heat isolation. The air temperature of the inner part of the waveguide can be measured as well. (c) An analyser is connected to the probes located in the front and rear ends of the waveguide, to collect the data for the S_{21} and S_{11} parameters

The purpose of the experiment was to test if the feature of the anapole state would indeed become apparent via the transmission characteristics that were obtained from the theoretical analysis presented in Sec. III B. In the experiment, a wave was probed, coupled to the TE_{10} mode of the waveguide, and guided onto the five water-filled cylinders; the cylinders then either reflected, transmitted or dissipated the power of the impinging wave. The amplitude and phase of the transmission coefficient S_{21} were measured for a specific temperature of the water. Then the same process was repeated when the water temperature was stabilized to a higher value. Beginning from 20^o and until the final value of 90^o, the data related to the S_{21} coefficient were collected. The frequency range of the transmission power lies from 1.4 GHz to 3.1 GHz and is presented in Fig. 17. In Fig. 17 it is interest-

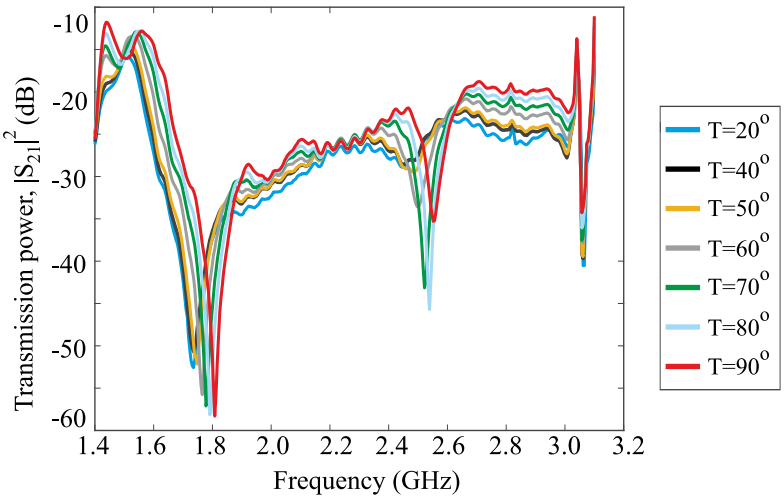

FIG. 17. Experimental data of the transmission power in dB for temperatures ranging from 20^o to 90^o. Notice that for temperatures lower than 50^o there is only one transmission peak in the range 1.4-1.6 GHz; this is in agreement with the theoretical results in Sec. III B. A second transmission peak in the corresponding frequency range appears distinctively for $T > 60^o$. The experimental spectral position of the first two peaks is also proven to be captured qualitative by the theoretical analysis that preceded.

ingly observed that the appearance of a second transmission peak around 1.4-1.6 GHz for temperature higher than $\sim 60^o$, coincides with the theoretical results of Sec. III B; in this range the anapole state is excited.

In order to demonstrate the true comparison of the theory and the experiment however, a waveguide was simulated with the exact dimensions as those of the WR430 design, as well as the permittivity, width and inner dimensions of the glass containers were taken into account. Using the Debye model of Eq. (5), for $T = 20^o$ the theoretical results from the waveguide simulation are compared to the experimental ones in Fig. 18(b); their agreement is excellent for $f < 2$ GHz. Another common feature is the improvement of the transmission with the increase of the temperature. Thus, having presented the experimental data, the previous theoretical analysis seems to capture the general qualitative features satisfactorily.

In Fig. 19 the transmission power obtained from the waveguide simulation is presented. The increase of the temperature improves the transmission as in the experiment, and a second peak appears in the spectrum near the frequencies 1.4-1.6 GHz. The position of the two first transmission peaks is also in relative accordance with the experimental observations. The theory however, suggests a larger dependence of the features in the temperature, as the curves are shifted more intensely to higher frequencies due to the temperature rise.

Many minor details are responsible for shaping the features of the experimental transmission power and provide explanations for the deviations amongst the theoretical and experimental results. For instance the actual value of the air gap above the five cylinders

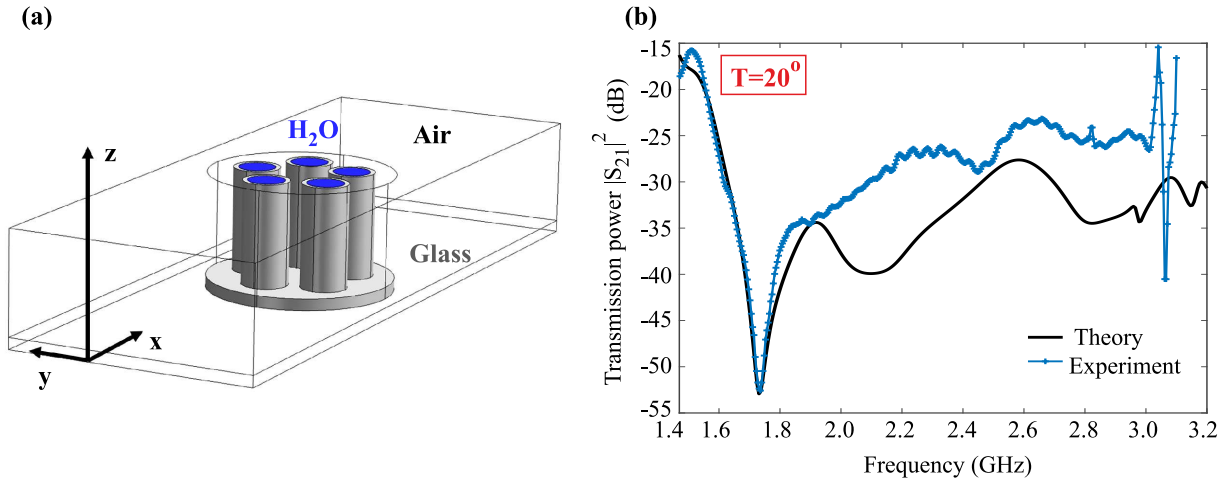

FIG. 18. (a) Schematics of the design in the simulation, employed to resemble the experiment as closely as possible. (b) Comparison of the experimental transmission power with the theoretical one, for water temperature 20^o. It is noticeable that the theory stands in excellent agreement for frequencies less than 2 GHz. Deviation is observed in the power at higher frequencies, but the overall tendency dictated by the theoretical simulations resembles closely the experiment. The consideration of the glass substrate on the bottom part of the five cylinders also affected significantly the S_{21} theoretical power.

within the waveguide (as it was stated that they were a little shorter from the inner height of the waveguide) was observed to affect importantly the theoretical results. The experimental data were also sensitive to the temperature variations, and when the measurement of the S_{21} coefficient was performed there could have been temporal temperature changes

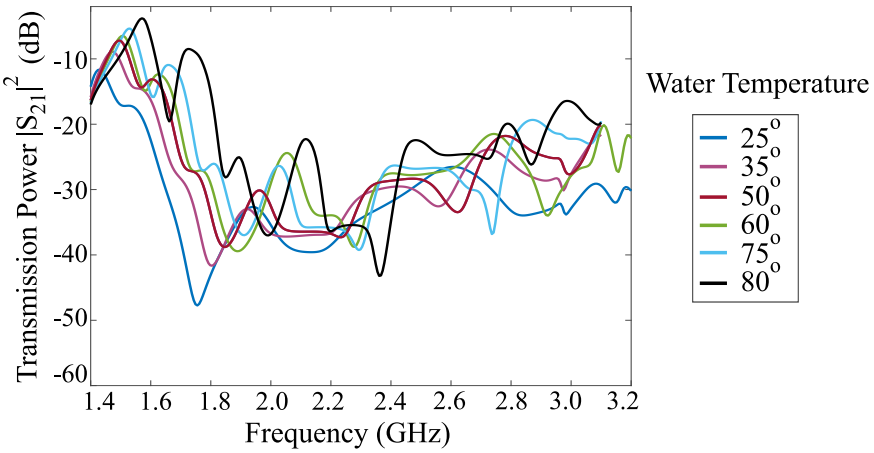

FIG. 19. Theoretical results of the transmission power obtained from the waveguide simulations, for various temperatures. There is a close agreement of theory and experiment, as the basic trend is reproduced. in the former the transmission peak around 1.4-1.6 GHz displays greater sensitivity to temperature variations and is shifted more to higher frequencies than the experiment.

that cannot be implemented in the theoretical simulations. Furthermore, it was the air temperature that was measured inside the waveguide close to the five cylinders, but not exactly the water temperature inside the configuration, which also accumulates an error in the theoretical analysis. Another reason for the existing discrepancies, could be the quality of the water; the potential presence of residual ions or impurities dynamically changes its properties, so deviations from the theoretical Debye model can also account for the differences between experiment and theory. Additional losses in the experiment may have occurred, since the theory suggests transmission $\sim 5-20\%$ greater than the experimental, for the high water temperatures that were studied.

The expectation of a transmission to the order of $\sim 60\%$ (based on Sec. III B for the infinite metasurface impinged by a plane wave), is significantly lower both in the experiment and waveguide simulation. This reveals that the deviation of the waveguide's mode from an actual plane wave has the major consequence of affecting the response of the unit-cell. Nevertheless, it is important that the experiment verified the expected characteristics that accompany the excitation of an anapole state.

Another possibility for more qualitative equivalence to an infinite metasurface impinged by a plane wave, would be to build a structure of a few repeated unit cells, and probe a wave that impacts onto the configuration. This could possibly recreate more accurately the results retrieved in the theoretical case of the infinite metasurface.

D. Conclusion

The characteristics and design principle of a many-rod water based metasurface, resilient enough for realistically implementing the anapole state, in the ever-present losses was presented. The enhanced toroidal moment originating from a collective toroidal supermode was exploited so as to attain the destructive interference between the electric and toroidal dipole moments. By means of optimization the, toroidal and electric dipole contributions were isolated from the contributions of other participants in the radiation, and the condition of the anapole was satisfied accurately. The controllability of the dielectric properties of water was realized by the temperature dependent water permittivity, was exploited to sustain and preserve the anapole state in the presence of losses. The theoretical analysis was further supported by a waveguide experiment, verifying the response of the metasurface when impinged by the TE_{10} waveguide mode, which possesses the closest resemblance to a plane wave. The tunable capabilities of water create an enhanced interest in exploring further its potential in water-based metamaterials. Combined with the new emergent phenomena that originate from the implementation of metamaterials, water has a lot to offer as a tuning mechanism not only for achieving the dynamic anapole state, but in a variety of other applications as well.

IV. APPENDIX

A. Causality in the connection between D and E fields

Causality is the fundamental feature of electromagnetic wave theory. It is the simple statement that the cause precedes the effect. In the relativistic theory it is referred to as the principle of relativistic causality which states that the signal cannot propagate with a velocity greater than the speed of light c in vacuum. The dielectric permittivity tensor is temporarily dispersive meaning that it depends upon the temporal angular frequency (i.e. $\tilde{\epsilon} = \epsilon(\omega)$). A temporary locally linear medium with no dispersion in frequency would imply an instantaneous connection between the induction fields **B**(**r**,t) and **E**(**r**,t) with the induced displacement vector **D**(**r**,t) and the magnetic intensity vector **H**(**r**,t) which is physically unreasonable [50].

A consequence of the frequency dependence of $\epsilon(\omega)$ is a temporally nonlocal connection between the displacement **D** and the **E** field [51]. If the monochromatic components of frequency ω are related by:

$$\mathbf{D}(\mathbf{r},\omega) = \epsilon(\omega)\mathbf{E}(\mathbf{r},\omega) \tag{6}$$

the dependence on time can be constructed by Fourier superpostition. Treating special coordinate as a parameter, the integrals are written as:

$$\mathbf{D}(\mathbf{r},t) = \frac{1}{\sqrt{2\pi}}\int_{-\infty}^{\infty}\mathbf{D}(\mathbf{r},\omega)e^{-i\omega t}d\omega \tag{7}$$

$$\mathbf{D}(\mathbf{r},\omega) = \frac{1}{\sqrt{2\pi}}\int_{-\infty}^{\infty}\mathbf{D}(\mathbf{r},t')e^{i\omega t'}dt' \tag{8}$$

with similar equations for the **E** field. Inserting the Eq. (6) into Eq. (7) gives:

$$\mathbf{D}(\mathbf{r},t) = \frac{1}{\sqrt{2\pi}}\int_{-\infty}^{\infty}\epsilon(\omega)\mathbf{E}(\mathbf{r},\omega)e^{-i\omega t}d\omega \tag{9}$$

Substituting the Fourier transform of the electric field $\mathbf{E}(\mathbf{r},\omega) = 1/(2\pi)^{1/2}\int_{-\infty}^{\infty}\mathbf{E}(\mathbf{r},t')e^{i\omega t'}dt'$, where t' is a time prior to time t (causal effect), into Eq. (9) yields:

$$\mathbf{D}(\mathbf{r},t) = \frac{1}{2\pi}\int_{-\infty}^{\infty}d\omega\epsilon(\omega)e^{-i\omega t}\int_{-\infty}^{\infty}dt'\mathbf{E}(\mathbf{r},t')e^{i\omega t'} \tag{10}$$

With the assumption that the orders of integration can be interchanged the last expression is written as:

$$\mathbf{D}(\mathbf{r},t) = \frac{1}{2\pi}\int_{-\infty}^{\infty}\int_{-\infty}^{\infty}d\omega dt'\epsilon(\omega)\mathbf{E}(\mathbf{r},t')e^{-i\omega(t-t')} \tag{11}$$

The dielectric function is related to the susceptibility by the expression $\epsilon(\omega) = \epsilon_0(1+\chi_\epsilon(\omega))$ and can be substituted into Eq. (11). Also recalling the integral representation of the delta function and the property $1/2\pi\int_{-\infty}^{\infty}f(t')e^{-i\omega(t-t')}dt' = f(t)$, Eq. (11) is written as:

$$\mathbf{D}(\mathbf{r},t) = \frac{1}{2\pi}\left\{\int_{-\infty}^{\infty}\int_{-\infty}^{\infty}d\omega dt'\epsilon_0\mathbf{E}(\mathbf{r},t')e^{-i\omega(t-t')}dt' + \int_{-\infty}^{\infty}\int_{-\infty}^{\infty}d\omega dt'\epsilon_0\chi_e(\omega)\mathbf{E}(\mathbf{r},t')e^{-i\omega\tau}dt'\right\} \tag{12}$$

And since $\chi_e(\omega) = \epsilon(\omega)/\epsilon + 0 - 1$ Eq. (12) takes the form:

$$\mathbf{D}(\mathbf{r},t) = \frac{1}{2\pi}\epsilon_0\mathbf{E}(\mathbf{r},t) + \int_{-\infty}^{\infty}\left\{\frac{1}{2\pi}\int_{-\infty}^{\infty}\left(\frac{\epsilon(\omega)}{\epsilon_0} - 1\right)e^{-i\omega\tau}d\omega\right\}\mathbf{E}(\mathbf{r},t-\tau)d\tau \tag{13}$$

where $\tau = t - t'$. In Eq. (13) the term in the brackets is the Fourier transform of the electric susceptibility which is denoted as $G(\tau) = 1/2\pi\int_{-\infty}^{\infty}(\frac{\epsilon(\omega)}{\epsilon_0} - 1)e^{-i\omega\tau}d\omega$, so finally the displacement vector reads:

$$\mathbf{D}(\mathbf{r},t) = \epsilon_0\left\{\mathbf{E}(\mathbf{r},t) + \int_{-\infty}^{\infty}G(\tau)\mathbf{E}(\mathbf{r},t-\tau)d\tau\right\} \tag{14}$$

Equation (14), as well as the Fourier transform of $G(\tau)$ give the nonlocal connection between **D** and **E**, and show the dependence of **D** on the electric field at another time t. When the dielectric function $\epsilon(\omega)$ has no dependence on ω for all values of ω it is easily retrieved that $G(\tau) \propto \delta(\tau)$ and therefore the instantaneous connection is obtained.

B. The Debye model of orientational polarization

The Lorentz model describes how the bounded electrons to the nucleus or lattice interact with electromagnetic field and generally oscillate about their equilibrium positions. Classically, the Newton's law is used to describe the oscillations by assuming a driving force, a spring force and a damping force [50]. The external driving force is due to the electric field, the spring force is the force exerted on the bound electrons to return to their equilibrium positions (and is zero for the case of dielectrics) and the damping force takes into account the decay of the oscillations. The Drude model is obtained by the Lorentz model, if one sets the resonant frequency of the oscillator to zero, as there are free electrons and no spring force "connects them" to the ions.

The Debye Model deals with another type of polarizing matter; it is associated with permanent dipoles rather than induced dipoles. The most distinctive example of a material that is comprised of permanent dipoles, is water. The water molecules have inherent randomly oriented dipole moments and when an electromagnetic field is applied, these tend to align along the direction of the external electromagnetic field. In this case, the restoring mechanism that tends to restore the dipoles to their equilibrium is the thermal motion which causes the randomization of the dipole orientations, opposing thus the effect of their alignment to the direction of the external field. This randomization is called relaxation. The relaxation process can be expressed as an exponential decrease in the polarization, since when the external field is turned of the material reaches equilibrium not instantaneously but over a period of time. The exponential decay of the polarization reads:

$$\mathbf{P}(t) = \mathbf{P}(0)e^{-t/\tau} \tag{15}$$

where τ is the relaxation time for the re-oritentation of the molecules. If the angular frequency ω of the applied field is much larger than τ^{-1} the molecules become unable to 'follow' the field. Debye proposed the decay function $\alpha(\omega) \propto e^{-t/\tau}$ describing the gradual decrease of the **D** field upon application of an external field **E**.

Assuming that at time t' an external field was turned on for a dt' interval, outside this interval the strength of the external field vanishes. The displacement **D** vector, in view of the inertia of the polarization **P** will persist at times $t > t' + dt'$, but will gradually vanish. Thus, **D** is a function of t and t' i.e.:

$$\mathbf{D}(t-t') = \mathbf{E}(t')\alpha(t-t')dt' \tag{16}$$

if $t > t' + dt'$. The decay function $\alpha(t-t') \rightarrow .$ if $t \rightarrow \infty$. The displacement vector contains a part that can follow the external field practically immediately, and which in view of the meaning of ϵ_∞ is equal to $\epsilon_\infty \mathbf{E}(t')$. Also, α is assumed to remain the same value $\alpha(0)$ during the short interval dt'. Thus:

$$\mathbf{D}(t-t') = \epsilon_\infty \mathbf{E}(t') + \mathbf{E}(t')\alpha(0)dt' \tag{17}$$

If another field $\mathbf{E}(t'')$ is assumed to be in effect at a later time $t'' = t' + dt''$ then by the principle of superposition the displacement field $\mathbf{D}(t-t'')$ is superposed linearly on the former one. If the $\mathbf{E}(t')$ field is applied to the material at time $t' = 0$, according to the principle of superposition the displacement $\mathbf{D}(t)$ field at time t becomes:

$$\mathbf{D}(t) = \epsilon_\infty \mathbf{E}(t) + \int_0 \mathbf{E}(t')\alpha(t-t')dt' \tag{18}$$

According to Debye's approach for how the molecules restore in their equilibrium the time derivative of the exponential decay function gives $d\alpha(t)/dt = -\tau^{-1}\alpha(t)$. By taking the time derivative of Eq. (18) and multiplying with τ one obtains [52]:

$$\tau \frac{d\mathbf{D}(t)}{dt} = \epsilon_\infty \tau \frac{d\mathbf{E}}{dt} + \tau\alpha(0)\mathbf{E} - \int_{-\infty}^{t} \mathbf{E}(t')\alpha(t-t')dt' \tag{19}$$

where the integral was safely extended to times $t < 0$ since the both the **D** and **E** fields vanish. Addition of Eq. (18) and (19) gives:

$$\tau \frac{d}{dt}(\mathbf{D} - \epsilon_\infty \mathbf{E}) + (\mathbf{D} - \epsilon_\infty \mathbf{E}) = \tau\alpha(0)\mathbf{E} \tag{20}$$

To determine $\alpha(0)$ the equilibrium condition is considered, so the time derivative is set to zero (equilibrium in a constant field), implying also $\mathbf{D} = \epsilon_s \mathbf{E}$. Therefore:

$$\alpha(0) = \frac{1}{\tau}(\epsilon_s - \epsilon_\infty) \tag{21}$$

Now, Eq. (20) is written as:

$$\tau \frac{d}{dt}(\mathbf{D} - \epsilon_\infty \mathbf{E}) + (\mathbf{D} - \epsilon_\infty \mathbf{E}) = (\epsilon_s - \epsilon_\infty)\mathbf{E} \tag{22}$$

Equation (22) becomes the differential equation connecting **D** with **E** under the assumption that the decay function is given by the equation $\alpha(t) = \tau^{-1}(\epsilon_s - \epsilon_\infty)e^{-t/\tau}$. Assuming a periodic field (i.e. $\mathbf{E} \propto e^{-i\omega t}$), then $d\mathbf{E}/dt = -i\omega\mathbf{E}$, $\mathbf{D} = \epsilon(\omega)\mathbf{E}$ and $d\mathbf{D}/dt = -i\omega\epsilon(\omega)\mathbf{E}$, so the differential Eq. (22) reads:

$$\tau(-i\omega\epsilon + i\omega\epsilon_\infty)\mathbf{E} + (\epsilon - \epsilon_\infty)\mathbf{E} = (\epsilon_s - \epsilon_\infty)\mathbf{E} \tag{23}$$

Thus, solving for $\epsilon(\omega)$ gives the Debye model for the dielectric function with one relaxation term:

$$\epsilon(\omega) - \epsilon_\infty = \frac{\epsilon_s - \epsilon_\infty}{1 - i\omega\tau} \tag{24}$$

The frequency dependence is expressed explicitly, but the temperature dependence appears implicitly through $\epsilon_s - \epsilon_\infty$ and τ, both of which usually depend on T. Solving for the real and imaginary parts of 24 one obtains:

$$\epsilon_1(\omega) - \epsilon_\infty = \frac{\epsilon_s - \epsilon_\infty}{1 + \omega^2\tau^2} \tag{25}$$

$$\epsilon_2(\omega) = \frac{(\epsilon_s - \epsilon_\infty)\omega\tau}{1 + \omega^2\tau^2} \tag{26}$$

Assuming that the Debye equations are fulfilled, $\tau(T)$ can be found from the frequency at which ϵ_2 has its maximum. In fact at a constant temperature the angular frequency ω_m of this maximum is determined by:

$$\frac{\partial\epsilon_2}{\partial\omega} = 0 \tag{27}$$

And since $\partial\epsilon_2/\partial\omega = 0$ when $\omega(T) = 1/\tau(T)$ from the first Eq. (27), so from the frequency at which ϵ_2 has its maximum one can find τ, or similarly it can either be retrieved from $\partial(\tan\phi)/\partial\omega = 0$, where $\tan\phi = \epsilon_2/\epsilon_1$ is the loss-angle ϕ. Then $\omega_{m,\phi}(T) = 1/\tau(T)(\epsilon_s/\epsilon_\infty)^{1/2}$, which is nearly equal to $\omega(T) = 1/\tau(T)$, for most substance for which the Debye equations can be expected to hold.

At the frequency when $\omega = \omega_m$ where ϵ_2 has its maximum the real and imaginary parts of the dielectric function become:

$$\epsilon_1 = \frac{1}{2}(\epsilon_s - \epsilon_\infty) \qquad\qquad \epsilon_2 = \frac{1}{2}(\epsilon_s - \epsilon_\infty) \tag{28}$$

An interesting feature of Eqs. (28) is that the values of ϵ_1 and ϵ_2 at the frequency ω_m are independent of this frequency and of the relaxation time; they only depend on ϵ_s and ϵ_∞. This gives a more clear insight about the meaning of ϵ_∞. According to the Debye equations ϵ_1 decreases from ϵ_s to ϵ_∞ in the frequency region in which ϵ_2 has relatively large values. Thus, it is the value which is asymptotically approached by ϵ_1 at frequencies sufficiently larger than $\omega = \omega_m$ to make ϵ_2 relatively small.

The Debye model that was used in the theoretical simulations is based on a model found in [36]:

$$\epsilon_0(T) = a_1 - b_1 T + c_1 T^2 - d_1 T^3 \tag{29}$$

$$\epsilon_\infty(T) = \epsilon_0(T) - a_2 e^{-b_2 T} \tag{30}$$

$$\tau(T) = c_2 e^{d_2/(T+T_0)} \tag{31}$$

where $a_1 = 87.9$, $b_1 = 0.404$ K^{-1}, $c_1 = 9.59 \times 10^{-4}$ K^{-2}, $d_1 = 1.33 \times 10^{-6}$ K^{-3}, $a_2 = 80.7$, $b_2 = 4.42 \times 10^{-3}$ K^{-1}, $c_2 = 1.37 \times 10^{-13}$ s, $d_2 = 651^o$ C, $T_0 = 133^o$ C and T is the water temperature in Celsius. The dependence of the parameters from the temperature as well as the constants, have been determined in many works by measurements performed on pure water.

The temperature of a material has significant effect on its dielectric properties. In general, the loss factor increases with increasing temperature at low frequencies due to ionic conductance, but decreases with increasing temperature at high frequencies due to free-water dispersion. Debye related the relaxation time for spherical molecule to viscosity and temperature as the result of randomizing agitation of the Brownian movement [53]:

$$\tau = V \frac{3v}{kT} \tag{32}$$

where v is the viscosity, V is the volume, k is the Boltzmann's constant and T is the temperature. For nonspherical water molecules the relation that holds is $\tau \propto v/T$, while the viscosity of all fluid decrease with increasing temperature exponentially i.e.:

$$v = v_0 e^{E_a/R_g T} \tag{33}$$

where E_a is the activation energy and R_g is the universal gas constant. The molecules in a liquid have no fixed positions. If a molecule momentarily is forced out of its equilibrium direction, its neighbours will tend to rearrange themselves in such a way so as to make this new direction an equilibrium position. Thus, there are two concepts about the way in which a dipole in a liquid alters its direction. It either jumps into a different direction, which requires that at least for the duration of the jump the arrangement of its neighbours should remain unaltered. The second is that such jumps occur rarely and that a dipole may change its direction only in conjunction with a rearrangement of the positions of the neighbours.

The description of the motion of these neighbouring molecules might be described by replacing them by a continuous medium with properties of a macroscopic viscous fluid. This indeed led Debye to introduce in his model the concept of a spherical dipolar molecule of radius a to be moving in a continuous viscous fluid with viscosity v and obeying the macroscopic equations of flow. The fluid is also considered to adhere to the surface of the molecule and on these assumptions the frictional constant of the sphere is given by Stokes's law ($\xi = 8\pi v a^3$).

Equation (33) is an empirical law for the viscosity and suggests that the jumps over a potential barrier of height E_α are carried out by the molecules of the liquid in processes connected with viscous flow.

As the temperature rises, the relaxation time decreases which means that the bonds break and reform much faster than in lower temperatures. The shifting of the relaxation time toward a lower value (which means that the frequency at the maximum $\Im(\epsilon)$ shifts toward a higher value as temperature increases) reduces the value of $\Im(\epsilon)$ for water at a fixed microwave frequency.

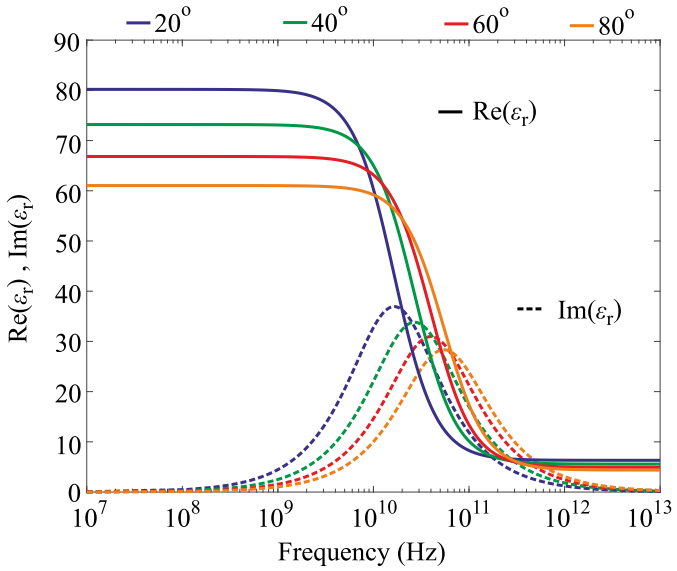

FIG. 20. Effect of the temperature on the dielectric constant $\epsilon_1 = \Re(\epsilon_r)$ and the loss factor $\epsilon_2 = \Im(\epsilon_r)$ of free water. Notice how the maximum of the loss factor is shifted to higher frequencies as the temperature rises, lowering thus the dissipation losses of water in the low GHz spectrum.

C. Expressions for calculating the moment terms of the multipole expansion

The decomposition of an E/M field that impinges in an infinite array of scatterers is presented in Savinov's work [43]. This decomposition results in certain mathematical quantities; the moments/multipole terms, and describe in this case the far field scattered by the infinite array. The summation of the far-field contributions of all moments at the position of the observer, effectively reconstructs the total scattered field. In all parts of the analysis, normal incidence was assumed along the $\hat{\mathbf{x}}$-axis and $\hat{\mathbf{z}}$ polarization of the impinging wave.

The scattered field by an isolated source is given by:

$$\mathbf{E}(\mathbf{r}) = \mathbf{E}_{(l=1)} + \mathbf{E}_{(l=2)} + \mathbf{E}_{(l=3)} + ...(l > 3) \tag{34}$$

where l is the angular momentum index of the spherical functions $Y_{l,m}$. The multipole expansion being a mathematical series is dependent on the angles θ, ϕ on a sphere. As the index l takes higher values, more information is acquired about the details of the angular characteristics of each order. For example, the l = 0 order does not depend on the angles and has a constant value. The next order l = 1 changes only once from positive to negative around the sphere, with higher orders being characterized by more abrupt variations [54].

When the current density $\mathbf{J}(r)$ distribution within the metaatom is calculated and the geometry is simple enough, an analytical expression can be extracted. The expression for the total scattered field, if all the unit cells are considered, reads:

$$\mathbf{E}_s = \sum_r \mathbf{E}(r) \approx \frac{1}{\Delta^2} \int_{array} d^2 r \mathbf{E}(r) \tag{35}$$

with Δ being the area of an individual unit cell. If one begins with the far-field distribution of each isolated multipole and using the spherical functions [43], it is proven that the equation for the scattered field is:

$$\begin{aligned}\mathbf{E}_s = \frac{\mu_o c^2}{2\Delta^2}\{&-ik\mathbf{p}_\parallel + ik\hat{\mathbf{R}}\times\left(\mathbf{m}_\parallel - \frac{k^2}{10}\mathbf{m}_\parallel^{(1)}\right) - k^2\left(\mathbf{T}_\parallel + \frac{k^2}{10}\mathbf{T}_\parallel^{(1)}\right) + k^2\left(\mathbf{Q}^{(e)}\cdot\hat{\mathbf{R}}\right)_\parallel \\ &- \frac{k^2}{2}\hat{\mathbf{R}}\times\left(\mathbf{Q}^{(m)}\cdot\hat{\mathbf{R}}\right)_\parallel - \frac{ik^3}{3}\left(\mathbf{Q}^{(T)}\cdot\hat{\mathbf{R}}\right)_\parallel + ik^3\left[\left(\mathbf{O}^{(e)}\cdot\hat{\mathbf{R}}\right)\cdot\hat{\mathbf{R}}\right]_\parallel \\ &- \frac{ik^3}{180}\hat{\mathbf{R}}\times\left[\left(\mathbf{O}^{(m)}\cdot\hat{\mathbf{R}}\right)\cdot\hat{\mathbf{R}}\right]_\parallel\}\times e^{(-ikR)}\end{aligned} \tag{36}$$

In the above expression, we recognize the electric, magnetic and toroidal dipoles ($\mathbf{p}_\parallel$, $\mathbf{m}_\parallel$, $\mathbf{T}_\parallel$) and the electric and magnetic quadrupoles ($\mathbf{Q}^{(e/m)}$) and octupoles ($\mathbf{O}^{(e/m)}$) respectively. The notation $\parallel$ means that the corresponding vector is parallel to the metasurface. In addition, the supersript $^{(1)}$ means that these moments are first order corrections (e.g. $\mathbf{m}_\parallel^{(1)}$ is a correction to the magnetic dipole moment $\mathbf{m}_\parallel$).

The analytical equations of the moments in Cartesian coordinates used in all parts of the thesis are provided below:

$$p_\alpha = \frac{1}{i\omega}\int d^3r J_\alpha \tag{37}$$

$$m_\alpha = \frac{1}{2c}\int d^3r\,[\mathbf{r}\times\mathbf{J}]_\alpha \tag{38}$$

$$T_\alpha = \frac{1}{10c}\int d^3r\left[(\mathbf{r}\cdot\mathbf{J})r_\alpha - 2r^2 J_\alpha\right] \tag{39}$$

$$Q^{(e)}_{\alpha,\beta} = \frac{1}{2i\omega}\int d^3r\left[r_\alpha J_\beta + r_\beta J_\alpha - \frac{2}{3}\delta_{\alpha,\beta}(\mathbf{r}\cdot\mathbf{J})\right] \tag{40}$$

$$Q^{(m)}_{\alpha,\beta} = \frac{1}{3c}\int d^3r\,[\mathbf{r}\times\mathbf{J}]_\alpha r_\beta + \{\alpha\leftrightarrow\beta\} \tag{41}$$

$$Q^{(T)}_{\alpha,\beta} = \frac{1}{28c}\int d^3r\left[4r_\alpha r_\beta(\mathbf{r}\cdot\mathbf{J}) - 5r^2\left(r_\alpha J_\beta + r_\beta J_\alpha\right) + 2r^2(\mathbf{r}\cdot\mathbf{J})\delta_{\alpha,\beta}\right] \tag{42}$$

$$\begin{aligned}O^{(e)}_{\alpha,\beta,\gamma} = \frac{1}{6i\omega}\int d^3r\left[J_\alpha\left(\frac{r_\beta r_\gamma}{3} - \frac{1}{5}r^2\delta_{\beta,\gamma}\right) + r_\alpha\left(\frac{J_\beta r_\gamma}{3} + \frac{J_\gamma r_\beta}{3} - \frac{2}{5}(\mathbf{r}\cdot\mathbf{J})\delta_{\beta,\gamma}\right)\right] \\ +\{\alpha\leftrightarrow\beta,\gamma\} + \{\alpha\leftrightarrow\gamma,\beta\}\end{aligned} \tag{43}$$

$$O^{(m)}_{\alpha,\beta,\gamma} = \frac{15}{2c}\int d^3r\left(r_\alpha r_\beta - \frac{r^2}{5}\delta_{\alpha,\beta}\right)\cdot[\mathbf{r}\times\mathbf{J}]_\gamma + \{\alpha\leftrightarrow\beta,\gamma\} + \{\alpha\leftrightarrow,\gamma,\beta\} \tag{44}$$

In order to clarify the above equations, it is imperative to find the multipole terms that contribute to the far-field scattering, for the case of the array orientation that has been studied in the previous sections. Each unit-cell is supposed to lay on the *yz* plane, recurring periodically along the $\hat{\mathbf{y}}$ axis. Moreover, the $\hat{\mathbf{z}}$-direction of the metasheet is extended to infinity. For the incident $\hat{\mathbf{z}}$-polarized plane wave, normal incidence is assumed and it translates along the $\hat{\mathbf{x}}$-direction.

The non-zero components of each multipole order, are evaluated based on the position of the observer. In this circumstance, the observer's position is $\hat{\mathbf{R}} = R\hat{\mathbf{x}}$. Then, for the magnetic dipole for instance, in order to get the component of the same polarization with the incident wave (and also lying onto the plane of the array) we have to find the projection of the vector onto the plane :

$$\mathbf{m}_{\parallel} = \mathbf{m} - \left(\mathbf{m}\cdot\hat{\mathbf{R}}\right)\cdot\hat{\mathbf{R}} = m_x\hat{\mathbf{x}} + m_y\hat{\mathbf{y}} + m_z\hat{\mathbf{z}} - m_x\hat{\mathbf{x}} = m_y\hat{\mathbf{y}} + m_z\hat{\mathbf{z}} \tag{45}$$

Now we return to the equation for the total scattered field. The equation reads: $\mathbf{E}_s \sim \hat{\mathbf{R}}\times\mathbf{m}_{\parallel} = \hat{\mathbf{x}}\times(m_y\hat{\mathbf{y}} + m_z\hat{\mathbf{z}}) = m_y\hat{\mathbf{z}} - m_z\hat{\mathbf{y}}$. However, from these two components m_y, m_z we want to keep only the one parallel to the polarization vector of the E-field, so the m_y component will contribute. In the same notion, the parallel components of the electric and toroidal dipoles are T_z and p_z. Continuing with the quadrupoles and using the Einstein summation convention we have:

$$\left(\mathbf{Q}^{(e)}\cdot\hat{\mathbf{R}}\right)_{\parallel} = \left(Q^{(e)}\hat{r_\alpha}(\hat{\mathbf{r}}\cdot\hat{\mathbf{x}})_\beta\right)_{\parallel} = \left(Q^{(e)}_{\alpha\beta}\hat{r_\alpha}\delta_{\beta x}\right)_{\parallel} = \left(Q^{(e)}_{\alpha x}\hat{r_\alpha}\right)_{\parallel} \tag{46}$$

Once again, we are only interested for the projection of the vector onto the plane of the unit-cell. So this means that $\alpha \to y$ or z. Then the above equation becomes:

$$\left(Q^{(e)}_{\alpha x}\hat{r_\alpha}\right)_{\parallel} = Q^{(e)}_{zx}\hat{\mathbf{z}} + Q^{(e)}_{yx}\hat{\mathbf{y}} \tag{47}$$

where we keep for the aforementioned reasons only the first term for the electric quadrupole. The same proof follows for the toroidal quadrupole ($Q^{(T)}$) term. For the magnetic quadrupole ($Q^{(m)}$) we deduce:

$$\begin{aligned}\hat{\mathbf{R}}\times\left(\mathbf{Q}^{(m)}\cdot\hat{\mathbf{R}}\right)_{\parallel} &= \hat{\mathbf{x}}\times\left(Q^{(m)}\hat{r_\alpha}(\hat{\mathbf{r}}\cdot\hat{\mathbf{x}})_\beta\right)_{\parallel} \\ &= \hat{\mathbf{x}}\times\left(Q^{(m)}_{\alpha\beta}\hat{r_\alpha}\delta_{\beta x}\right)_{\parallel} = \hat{\mathbf{x}}\times\left(Q^{(m)}_{\alpha x}\hat{r_\alpha}\right)_{\parallel} \\ &= \hat{\mathbf{x}}\times\left(Q^{(m)}_{zx}\hat{\mathbf{z}} + Q^{(m)}_{yx}\hat{\mathbf{y}}\right) = -Q^{(m)}_{zx}\hat{\mathbf{y}} + Q^{(m)}_{yx}\hat{\mathbf{z}}\end{aligned} \tag{48}$$

where we result in $Q^{(m)}_{yx}$ term.

For the electric octupole:

$$\left[\left(\mathbf{O}^{(e)}\cdot\hat{\mathbf{R}}\right)\cdot\hat{\mathbf{R}}\right]_{\parallel} = \left(O^{(e)}_{\alpha\beta\gamma}\hat{r_\alpha}\delta_{\beta x}\delta_{\gamma x}\right)_{\parallel} = O^{(e)}_{zxx}\hat{\mathbf{z}} + O^{(e)}_{yxx}\hat{\mathbf{y}} \tag{49}$$

so the moment of interest is $O^{(e)}_{zxx}$. Finally, for the magnetic octupole the equation reads:

$$\hat{\mathbf{R}}\times\left[\left(\mathbf{O}^{(m)}\cdot\hat{\mathbf{R}}\right)\cdot\hat{\mathbf{R}}\right]_{\parallel} = \hat{\mathbf{x}}\times\left(O^{(m)}_{\alpha\beta\gamma}\hat{r_\alpha}\delta_{\beta x}\delta\gamma x\right)_{\parallel} = \hat{\mathbf{x}}\times\left(O^{(m)}_{zxx}\hat{\mathbf{z}} + O^{(m)}_{yxx}\hat{\mathbf{y}}\right) = -O^{(m)}_{zxx}\hat{\mathbf{y}} + O^{(m)}_{yxx}\hat{\mathbf{z}}. \tag{50}$$

so the last term satisfies the above conditions.

D. Waveguides and Cutoff frequency

Consider a hollow waveguide with z being the axis along the length of the waveguide and xz plane parallel to any cross-sectional surface of the waveguide [51]. Beginning from the Maxwell's equations for the **E** and **B** fields and assuming a sinusoidal time dependence $e^{-i\omega t}$ the equations take the forms:

$$\nabla \times \mathbf{E} = i\omega\mathbf{B} \qquad \nabla \times \mathbf{B} = 0 \tag{51}$$

$$\nabla \cdot \mathbf{B} = -i\mu\epsilon\omega\mathbf{E} \qquad \nabla \cdot \mathbf{E} = 0 \tag{52}$$

Application of the curl operator $\nabla\times$ on the curl equations for the **E** and **B** fields yields the Helmholtz equations:

$$(\nabla^2 + \mu\epsilon\omega^2)\begin{Bmatrix}\mathbf{E}\\ \mathbf{B}\end{Bmatrix} = 0 \tag{53}$$

The waves propagates along the z direction, along the length of the waveguide so the fields can be written as:

$$\begin{Bmatrix}\mathbf{E}(x,y,z,t)\\ \mathbf{B}(x,y,z,t)\end{Bmatrix} = \begin{Bmatrix}\mathbf{E}(x,y)e^{\pm ikz-i\omega t}\\ \mathbf{B}(x,y)e^{\pm ikz-i\omega t}\end{Bmatrix} \tag{54}$$

Now the fields can be decomposed into parallel and transverse components with respect to the propagation along the $\hat{\mathbf{z}}$ axis:

$$\mathbf{E} = \mathbf{E}_\mathrm{z} + \mathbf{E}_\mathrm{t} \tag{55}$$

where $\mathbf{E}_\mathrm{z} = \hat{\mathbf{z}}E_\mathrm{z}$ and $\mathbf{E}_\mathrm{t} = (\hat{\mathbf{z}} \times \mathbf{E}) \times \hat{\mathbf{z}}$. In order to separate into transverse and parallel components the laplacian operator is written as $\nabla^2 = \nabla_\mathrm{t}^2 + \partial^2/\partial z^2$.

Beginning from the divergence equations for the **E** field:

$$\nabla \cdot \mathbf{E} = 0 \Rightarrow (\nabla_\mathrm{t} + \hat{\mathbf{k}}\frac{\partial}{\partial z}) \cdot (\mathbf{E}_\mathrm{t} + \hat{\mathbf{k}}E_\mathrm{z}) = 0 \Rightarrow \nabla_\mathrm{t} \cdot \mathbf{E}_\mathrm{t} + \frac{\partial E_\mathrm{z}}{\partial z} = 0 \tag{56}$$

And similarly for the **B** field.

$$\nabla_\mathrm{t} \cdot \mathbf{B}_\mathrm{t} + \frac{\partial B_\mathrm{z}}{\partial z} = 0 \tag{57}$$

For the curl equation of the electric field one obtains:

$$\nabla_\mathrm{t} \times \mathbf{E}_\mathrm{t} + \nabla_\mathrm{t} \times \hat{\mathbf{k}}E_\mathrm{z} + \hat{\mathbf{k}} \times \frac{\partial \mathbf{E}_\mathrm{t}}{\partial z} = i\omega\mathbf{B}_\mathrm{t} + i\omega\hat{\mathbf{k}}B_\mathrm{z} \tag{58}$$

In Eq. (56), one recognizes that the first term in the LHS and the second term in the RHS are parallel to the propagation of the waveguide, while the rest of the terms are perpendicular. Therefore:

$$\nabla_\mathrm{t} \times \mathbf{E}_\mathrm{t} = i\omega\hat{\mathbf{k}}B_\mathrm{z} \qquad \nabla_\mathrm{t} \times \hat{\mathbf{k}}E_\mathrm{z} + \hat{\mathbf{k}} \times \frac{\partial \mathbf{E}_\mathrm{t}}{\partial z} = i\omega\mathbf{B}_\mathrm{t} \tag{59}$$

The second expression in Eq. (59) is written as:

$$(\hat{\mathbf{i}}\times\hat{\mathbf{k}})\frac{\partial E_z}{\partial x}+(\hat{\mathbf{j}}\times\hat{\mathbf{k}})\frac{\partial E_z}{\partial y}+\hat{\mathbf{k}}\times\frac{\partial \mathbf{E}_t}{\partial z}=i\omega\mathbf{B}_t \Rightarrow -\hat{\mathbf{j}}\frac{\partial E_z}{\partial x}+\hat{\mathbf{i}}\frac{\partial E_z}{\partial y}+\hat{\mathbf{k}}\times\frac{\partial \mathbf{E}_t}{\partial z}=i\omega\mathbf{B}_t \tag{60}$$

Applying $\hat{\mathbf{k}}\times$ on Eq. (60) gives:

$$\hat{\mathbf{i}}\frac{\partial E_z}{\partial x}+\hat{\mathbf{j}}\frac{\partial E_z}{\partial y}-\frac{\partial \mathbf{E}_t}{\partial z}=i\omega(\hat{\mathbf{k}}\times\mathbf{B}_t)\Rightarrow\frac{\partial \mathbf{E}_t}{\partial z}+i\omega\hat{\mathbf{k}}\times\mathbf{B}_t=\nabla_t E_z \tag{61}$$

Similarly for the $\mathbf{B}$ field the curl equation reads:

$$\nabla_t\times\mathbf{B}_t+\nabla_t\times\hat{\mathbf{k}}B_z+\hat{\mathbf{k}}\times\frac{\partial \mathbf{B}_t}{\partial z}=-i\mu\epsilon\omega\mathbf{E}_t-i\mu\epsilon\omega\hat{\mathbf{k}}E_z \tag{62}$$

Once again separating the parallel and transverse components gives:

$$\nabla_t\times\mathbf{B}_t=-i\mu\epsilon\omega\hat{\mathbf{k}}E_z \qquad\qquad \nabla_t\times\hat{\mathbf{k}}B_z+\hat{\mathbf{k}}\times\frac{\partial \mathbf{B}_t}{\partial z}=-i\mu\epsilon\omega\mathbf{E}_t \tag{63}$$

Applying $\hat{\mathbf{k}}\times$ on Eq. (63) yields:

$$(\hat{\mathbf{i}}\times\hat{\mathbf{k}})\frac{\partial B_z}{\partial x}+(\hat{\mathbf{j}}\times\hat{\mathbf{k}})\frac{\partial B_z}{\partial y}+\hat{\mathbf{k}}\times\frac{\partial \mathbf{B}_t}{\partial z}\times\hat{\mathbf{k}}=-i\mu\epsilon\omega\hat{\mathbf{k}}\times\mathbf{E}_t\Rightarrow-\hat{\mathbf{j}}\frac{\partial B_z}{\partial z}+\hat{\mathbf{i}}\frac{\partial B_z}{\partial z}+\hat{\mathbf{k}}\frac{\partial \mathbf{B}_t}{\partial z}=-i\mu\epsilon\omega\hat{\mathbf{k}}\times\mathbf{E}_t \tag{64}$$

Therefore:

$$\nabla_t B_z=-i\omega\mu\epsilon(\hat{\mathbf{k}}\times\mathbf{E}_t)+\frac{\partial \mathbf{B}_t}{\partial z} \tag{65}$$

All equations collectively for the decomposition in transverse and parallel components to the $\hat{\mathbf{z}}$ axis propagation are:

$$\nabla_t\cdot\mathbf{B}_t+\frac{\partial B_z}{\partial z}=0 \qquad\qquad \nabla_t\cdot\mathbf{E}_t+\frac{\partial E_z}{\partial z}=0 \tag{66}$$

$$\nabla_t\times\mathbf{B}_t=-i\mu\epsilon\omega\hat{\mathbf{k}}E_z \qquad\qquad \nabla_t B_z=-i\omega\mu\epsilon(\hat{\mathbf{k}}\times\mathbf{E}_t)+\frac{\partial \mathbf{B}_t}{\partial z} \tag{67}$$

$$\nabla_t\times\mathbf{E}_t=i\omega\hat{\mathbf{k}}B_z \qquad\qquad \frac{\partial \mathbf{E}_t}{\partial z}+i\omega\hat{\mathbf{k}}\times\mathbf{B}_t=\nabla_t E_z \tag{68}$$

From the second expression of Eq. (53) solving in terms of $\mathbf{B}_t$ gives:

$$\mathbf{B}_t=\frac{i}{\omega^2\mu\epsilon-k^2}(k\nabla_t B_z+\omega\mu\epsilon\hat{\mathbf{k}}\times\nabla_t E_z) \tag{69}$$

and solving in terms of $\mathbf{E}_t$ in the second expression of Eq. (52) gives:

$$\mathbf{E}_t=\frac{i}{\omega^2\mu\epsilon-k^2}\left\{k\nabla_t E_z-\omega\hat{\mathbf{k}}\times\nabla_t B_z\right\} \tag{70}$$

Now, the Helmholtz equations need to be solved (i.e. $\left\{\nabla_t^2+\omega^2\mu\epsilon-k^2\right\}E_z$ and similarly for the B_z component) and from Eqs. (69), (70) the complete solution can be obtained.

For a perfect conductor the boundary conditions from the Maxwell's equations result in:

$$\hat{\mathbf{n}}\times\mathbf{E}=0 \qquad\qquad \hat{\mathbf{n}}\cdot\mathbf{B}=0 \tag{71}$$

where $\hat{\mathbf{n}}$ is the unit normal at the surface S. Thus, on the surface, the tangential (along the $\hat{\mathbf{z}}$-axis component) $E_z|_S = 0$ and the normal derivative of the $\mathbf{B}$ field is also zero, $\partial B_z/\partial n|_S = 0$. The extra condition for a transverse electric is that there cannot be E_z component anywhere, since this is the propagation of the wave. From the Helmholtz equation for B_z by denoting $\gamma^2 = \mu\epsilon\omega^2 - k^2$, one has to solve"

$$\nabla_t^2 B_z = -\gamma^2 B_z \tag{72}$$

which is simply an eigenvalue problem with eigenvalues $\gamma_\lambda^2 = \mu\epsilon\omega^2 - k_\lambda^2$. In order for the solution to be oscillatory and not decaying implies $\gamma^2 > 0 \Rightarrow \omega \geqslant \gamma_\lambda/\sqrt{\mu\epsilon}$, where $\omega_\lambda = \gamma_\lambda/\sqrt{\mu\epsilon}$ is the cutoff frequency. So the wave number becomes $k_\lambda = \mu\epsilon(\omega^2 - \omega_\lambda^2)^{1/2}$, and it is shown that for $\omega < \omega_\lambda$ the wave number is imaginary; this means that such mode cannot propagate and is called cutoff or evanescent mode.

For a rectangular waveguide (and TE modes) the Helmholtz equation reads:

$$\left(\frac{\partial^2}{\partial x^2} + \frac{\partial^2}{\partial y^2} + \gamma^2\right) B_z = 0 \tag{73}$$

with boundary conditions $E_z = 0$ everywhere, and $\partial B_z/\partial n = 0$ at $x = 0, a$ and $y = 0, b$ (see Fig. 21).

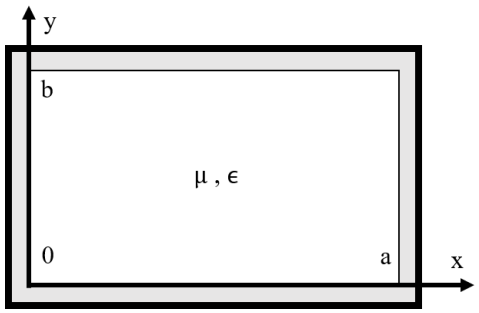

FIG. 21. Schematics of the cross-section of a rectangular waveguide. The boundary conditions for TE modes is $\partial B_z/\partial n = 0$ at $x = 0, a$ and $y = 0, b$ and $E_z = 0$ everywhere.

The solution is easily retrieved by separation of variables:

$$B_{mn} = B_0 \cos\left(\frac{m\pi x}{a}\right) \cos\left(\frac{n\pi y}{b}\right) \tag{74}$$

where α is the width of the waveguide and b is the height. Also, the eignevalues are given by:

$$\gamma_{mn}^2 = \pi^2 \left(\frac{m^2}{a^2} + \frac{n^2}{b^2}\right) \tag{75}$$

and the cutoff frequencies by:

$$\omega_{mn} = \frac{\pi}{\sqrt{\mu\epsilon}} \left(\frac{m^2}{a^2} + \frac{n^2}{b^2}\right)^{1/2} \tag{76}$$

For $a > b$ the lowest cutoff frequency, that of the dominant TE mode occurs for $m = 1$ and $n = 0$, and is equal to $\omega_{10} = \pi/\sqrt{\mu\epsilon}a$. For the WR430 waveguide with $\epsilon = 8.85 \times 10^{-12}$ F/m, $\mu = 4\pi \times 10^{-7}$ H/m and $a = 109.22$ mm the angular cutoff frequency of the TE_{10} mode is $\omega_{10} = 8.6252 \times 10^9$ rad/s and the cutoff frequency $f_{10} = 1.3727$ GHz.

[1] A. J. Devaney and E. Wolf, Phys. Rev. D **8**, 1044 (1973).

[2] K. Kim and E. Wolf, Opt. Commun. **59**, 1 (1986).

[3] K. Koshelev, G. Favraud, A. Bogdanov, Y. Kivshar, and F. A., Nanophotonics (2019).

[4] K. V. Baryshnikova, D. A. Smirnova, B. S. Luk'yanchuk, and Y. S. Kivshar, Adv. Opt. Mater. **0**, 1801350 (2019).

[5] G. N. Afanasiev and Y. P. Stepanovsky, J. Phys. A Math. Gen. **28**, 4565 (1995).

[6] V. M. Dubovik and V. V. Tugushev, Phys. Rep. **187**, 145 (1990).

[7] E. E. Radescu and G. Vaman, Phys. Rev. E Stat. Phys. Plasmas Fluids Relat. Interdiscip. Topics **65**, 47 (2002).

[8] T. Kaelberer, V. A. Fedotov, N. Papasimakis, D. P. Tsai, and N. I. Zheludev, Science **330**, 1510 (2010).

[9] N. Papasimakis, V. A. Fedotov, T. A. Savinov, V. Raybould, and N. I. Zheludev, Nat. Mater. **15**, 263 (2016).

[10] N. A. Nemkov, A. A. Basharin, and V. A. Fedotov, Phys. Rev. B **95**, 165134 (2017).

[11] V. A. Fedotov, A. V. Rogacheva, V. Savinov, D. P. Tsai, and N. I. Zheludev, Sci. Rep. **3**, 2967 (2013).

[12] A. E. Miroshnichenko, A. B. Evlyukhin, Y. F. Yu, R. M. Bakker, A. Chipouline, A. I. Kuznetsov, B. Luk'yanchuk, B. N. Chichkov, and Y. S. Kivshar, Nat. Commun. **6**, 8069 (2015).

[13] W. Liu, J. Zhang, B. Lei, H. Hu, and A. E. Miroshnichenko, Opt. Lett. **40**, 2293 (2015).

[14] L. Wei, Z. Xi, N. Bhattacharya, and H. P. Urbach, Optica **3**, 799 (2016).

[15] B. Luk'yanchuk, R. Paniagua-Domínguez, A. I. Kuznetsov, A. E. Miroshnichenko, and Y. S. Kivshar, Phys. Rev. A **95**, 063820 (2017).

[16] W. Liu and A. E. Miroshnichenko, Laser Photonics Rev. **11**, 1700103 (2017).

[17] G. Grinblat, Y. Li, M. P. Nielsen, R. F. Oulton, and S. A. Maier, Nano Lett. **16**, 4635 (2016).

[18] G. Grinblat, Y. Li, M. P. Nielsen, R. F. Oulton, and S. A. Maier, ACS Nano **11**, 953 (2017).

[19] G. Grinblat, Y. Li, M. P. Nielsen, R. F. Oulton, and S. A. Maier, ACS Photonics **4**, 2144 (2017).

[20] J. S. Totero Gongora, S. Juan, A. E. Miroshnichenko, Y. S. Kivshar, and A. Fratalocchi, Nat. Commun. **8**, 15535 (2017).

[21] S. Liu, Z. Wang, W. Wang, J. Chen, and Z. Chen, Opt. Express **25**, 22375 (2017).

[22] A. K. Ospanova, I. V. Stenishchev, and A. A. Basharin, Laser Photonics Rev. **12**, 1800005 (2018).

[23] J. F. Algorri, D. C. Zografopoulos, A. Ferraro, B. García-Cámara, R. Vergaz, R. Beccherelli, and J. M. Sánchez-Pena, Nanomaterials **9**, 30 (2018).

[24] D. G. Baranov, R. Verre, P. Karpinski, and M. Käll, ACS Photonics **5**, 2730 (2018).

[25] V. A. Zenin, A. B. Evlyukhin, S. M. Novikov, Y. Yang, R. Malureanu, A. V. Lavrinenko, B. N. Chichkov, and S. I. Bozhevolnyi, Nano Lett. **17**, 7152 (2017).

[26] Y. Yang, V. A. Zenin, and S. I. Bozhevolnyi, ACS Photonics **5**, 1960 (2018).

[27] Z. Dong, J. Zhu, J. Rho, J. Li, C. Lu, X. Yin, and X. Zhang, Appl. Phys. Lett. **101**, 1 (2012).

[28] Z. Liu, S. Du, A. Cui, Z. Li, Y. Fan, S. Chen, W. Li, J. Li, and C. Gu, Adv. Mater. **29**, 1606298

(2017).

[29] A. Sayanskiy, M. Danaeifar, P. Kapitanova, and A. E. Miroshnichenko, Adv. Opt. Mater. **6**, 1800302 (2018).

[30] O. Tsilipakos, A. C. Tasolamprou, T. Koschny, M. Kafesaki, E. N. Economou, and C. M. Soukoulis, Adv. Opt. Mater. **6**, 1800633 (2018).

[31] A. C. Tasolamprou, O. Tsilipakos, M. Kafesaki, C. M. Soukoulis, and E. N. Economou, Phys. Rev. B **94**, 205433 (2016).

[32] T. C. Huang, B. X. Wang, and C. Y. Zhao, J. Appl. Phys. **125**, 093102 (2019).

[33] A. A. Basharin, M. Kafesaki, E. N. Economou, C. M. Soukoulis, V. A. Fedotov, V. Savinov, and N. I. Zheludev, Phys. Rev. X **5**, 011036 (2015).

[34] A. C. Tasolamprou, O. Tsilipakos, A. A. Basharin, M. Kafesaki, C. M. Soukoulis, and E. N. Economou, *Toroidal Multipoles in Metamaterials* (World Scientific, "in press").

[35] O. Tsilipakos, A. C. Tasolamprou, T. Koschny, M. Kafesaki, E. N. Economou, and C. M. Soukoulis, in *2017 11th Int. Cong. Eng. Mater. Platforms for Nov. Wave Phenomena (Metamaterials)* (2017) pp. 355–357.

[36] A. Andryieuski, S. M. Kuznetsova, S. V. Zhukovsky, Y. S. Kivshar, and A. V. Lavrinenko, Scientific Reports **5**, 13535 EP (2015), article.

[37] E. Motovilova, S. Sandeep, M. Hashimoto, and S. Y. Huang, (2019).

[38] Y. Pang, J. Wang, Q. Cheng, S. Xia, X. Y. Zhou, Z. Xu, T. J. Cui, and S. Qu, Applied Physics Letters **110**, 104103 (2017).

[39] J. Zhao, S. Wei, C. Wang, K. Chen, B. Zhu, T. Jiang, and Y. Feng, Opt. Express **26**, 8522 (2018).

[40] A. V. Lavrinenko, R. E. Jacobsen, S. Arslanagic, S. Kuznetsova, A. Andryieuski, M. Odit, and P. Kapitanova, in *2017 47th European Microwave Conference (EuMC)* (2017) pp. 492–495.

[41] X. Sun, Q. Fu, Y. Fan, H. Wu, K. Qiu, R. Yang, W. Cai, N. Zhang, and F. Zhang, Scientific Reports **9**, 5417 (2019).

[42] "Comsol multiphysics," https://www.comsol.com/.

[43] V. Savinov, V. A. Fedotov, and N. I. Zheludev, Phys. Rev. B **89**, 205112 (2014).

[44] Journal of the Society of Chemical Industry **48**, 1036 (1929).

[45] W. J. Ellison, Journal of Physical and Chemical Reference Data **36**, 1 (2007).

[46] P. W. Rosenkranz, Geoscience and Remote Sensing, IEEE Transactions on **53**, 1387 (2015).

[47] A. A. Basharin, M. Kafesaki, E. N. Economou, C. M. Soukoulis, V. A. Fedotov, V. Savinov, and N. I. Zheludev, Phys. Rev. X **5**, 011036 (2015).

[48] I. V. Stenishchev and A. A. Basharin, Scientific Reports **7**, 9468 (2017).

[49] "Waveguide(electromagnetism)," https://en.wikipedia.org/wiki/Waveguide_(electromagnetism).

[50] C. D. Sarris, IEEE Antennas and Propagation Magazine **52**, 116 (2010).

[51] J. D. Jackson, *Classical electrodynamics*, 3rd ed. (Wiley, New York, NY, 1999).

[52] H. Frohlich, *Theory of dielectrics : dielectric constant and dielectric loss*, 2nd ed. (Clarendon Press Oxford, 1958).

[53] E. N. IVANOV, Sov. Phys. JETP **18**, 1509 (1963).

[54] "Multipole expansion," https://en.wikipedia.org/wiki/Multipole_expansion.